

Thermal and mechanical properties and the structural phase transition under pressure in $A\text{In}_2\text{As}_2$ ($A = \text{Ca}, \text{Sr}, \text{Ba}$)

Wen-Ti Guo , Zhigao Huang , and Jian-Min Zhang ^{*}

Fujian Provincial Key Laboratory of Quantum Manipulation and New Energy Materials, College of Physics and Energy, Fujian Normal University, Fuzhou 350117, China
and Fujian Provincial Collaborative Innovation Center for Advanced High-Field Superconducting Materials and Engineering, Fuzhou 350117, China

 (Received 29 May 2023; revised 3 August 2023; accepted 1 September 2023; published 25 September 2023)

Experimental results that BaIn_2As_2 and $\text{Ca}(\text{Sr})\text{In}_2\text{As}_2$, which are the same class of alkali metal compounds, belong to different structural phases have puzzled the current materials physics community. Here, we investigate the pressure-induced structural phase transition of $A\text{In}_2\text{As}_2$ and its accompanying improvement in mechanical and thermal properties. Firstly, the structural stability of the materials and their structural phase transitions under pressure are characterized by enthalpy and double checked by phonon dispersion spectrum. We also confirm the structural phase transitions of the hexagonal and monoclinic phases from a group-theoretic point of view, associating their symmetry operations using transformation matrices. In terms of mechanical properties, we propose an effective scheme for pressure modulation of the anisotropy of $A\text{In}_2\text{As}_2$ materials and to induce the transformation of $A\text{In}_2\text{As}_2$ from isotropic to anisotropic (hexagonal) and from brittle to ductile (hexagonal and monoclinic). Meanwhile, we find the negative Poisson's ratio phenomenon under compression and tension, which is favorable for a wide range of applications of this series of materials in aerospace, medicine, sensors, etc. In terms of thermal properties, applying pressure will enhance the structural phase transition temperature of $A\text{In}_2\text{As}_2$ materials to near room temperature. We further give direct evidence of phonon softening based on group velocity calculations and reveal that phonon softening prevents the heat capacity from reaching the Dulong-Petit limit. Our study provides a theoretical basis for selecting stable structural phases and pioneering thermodynamic property studies of the thermoelectric topological candidate material $A\text{In}_2\text{As}_2$.

DOI: [10.1103/PhysRevB.108.094111](https://doi.org/10.1103/PhysRevB.108.094111)

I. INTRODUCTION

EuX_2As_2 ($X = \text{Cd}, \text{In}, \text{Sn}$), as a series of topologically magnetic material, has been of great interest to topological thermoelectric community because of the intrinsically novel properties. The layered structure of the Zintl-Klemm phase, EuSn_2As_2 , can be easily peeled off [1]. Both theoretical and experimental-based studies have demonstrated that it is an intrinsically magnetic topological insulator [2]. Other related studies applied high pressure modulation of EuSn_2As_2 material to achieve a continuous transition from $R\bar{3}m$ phase to $C2/m$ phase [3], and to the high-pressure rhombohedral phase [4]. In addition, EuCd_2As_2 is considered to be a Dirac semimetal [5–7]. It will undergo a topological phase transition by reforming the magnetic moment direction under the action of pressure [5] or an electric field [8]. Similarly, as an intrinsic magnetic topological insulator, EuIn_2As_2 has higher-order topological insulator and axion insulator features [9–13]. It also exhibits magnetic configuration-dependent topological phase transition [12–14].

Alkaline earth (A) metal substituted Eu positions will achieve rich nonmagnetic topological states, which are reflected in both $\text{Sr}(\text{Ba})\text{Cd}_2\text{As}_2$ [15–17] and SrSn_2As_2 [18,19].

Likewise, our previous paper reported that $A\text{In}_2\text{As}_2$ ($A = \text{Ca}, \text{Sr}, \text{Ba}$) can achieve both metal-insulator phase transitions and topological quantum phase transitions under the action of pressure [20]. Meanwhile, CaIn_2As_2 and SrIn_2As_2 have been reported to have a $P6_3/mmc$ phase, while BaIn_2As_2 possesses a $P2/m$ phase [21]. Why do compounds of Ba, also an alkaline earth metal, behave in a different phase to compounds of Ca and Sr? This is a key question that needs to be urgently explored. Perhaps there are structural phase transitions between them? If there exists structural phase transition, what is the pattern? Are there other intrinsic physical properties that might accompany them? These are the crucial questions that have plagued the experimental field and the reasons that have stimulated research into them in the field of theoretical computing.

As a key means of experimentally regulating the physical properties of materials, pressure is also a research method of particular interest for theoretical calculations. Pressure often induces interesting and important potential properties in materials. For example, a topological phase transition will be achieved by applying hydrostatic pressure in MnBi_2Te_4 [22,23] and Cd_3As_2 [24,25]. The pressure will also obtain a metal-insulator phase transition accompanied by a change in the band gap [26–28]. In general, the application of pressure inevitably results in structural phase changes. Hydrostatic pressure modulation of the MnBi_4Te_7 appears as a structural

^{*}Corresponding author: jmzhang@fjnu.edu.cn

phase transition [22]. Tensile and compressive strains lead to multiple phase transitions in photovoltaic films CsMI_3 ($M = \text{Pb}, \text{Sn}$) [29]. Related studies have reported that narrow bandgap SrX_2As_2 ($X = \text{Cd}, \text{Sn}$) materials are easily modulated by external fields [16,18]. Pressure is an effective means of studying the properties and relationships between the different structural phases of a material.

Here, we apply pressure to AlIn_2As_2 with three different structural phases ($P6_3/mmc$, $R\bar{3}m$, and $P2/m$) to achieve materials rich in structural phase transition. CaIn_2As_2 and SrIn_2As_2 exhibit a $P6_3/mmc$ or $R\bar{3}m$ phase at low pressure, which transforms into a $P2/m$ phase with increasing pressure. However, BaIn_2As_2 tends to form a $P2/m$ phase. The phases of the three materials are in agreement with the reported experimental results [21]. The stability of these phases is next determined by phonon spectral calculations. And we further analyzed the change of the phonon irreducible representation of the pressure-induced structural phase transition. Furthermore, we have investigated the effect of hydrostatic pressure on the mechanical and thermodynamic properties of the material. Our paper explains the physical properties of the structural phase differences between BaIn_2As_2 and CaIn_2As_2 (SrIn_2As_2) and assesses their structural stability and thermal and mechanical characteristics.

A brief synopsis of the subsequent content of this paper is given here. Section II presents the crystal structures and detailed calculations of DFT. Section III focuses on the results of the study and discussion. Sections III A 1 investigates the energy and lattice structure characterization at different pressures and proposes structural phase transitions. Sections III A 2 investigates the structural phase transitions in pressure-modulated systems employing phonon spectroscopy. Sections III A 3 explains the physical nature of structural phase transitions utilizing symmetry shifts in point groups. Subsection III B focuses on the mechanical and thermal properties of materials under pressure modulation. Sections III B 1 analyses the crystalline anisotropy of the material. Sections III B 2 characterizes the material's thermal properties and discusses the realization of negative Poisson's ratio (NPR) performance modulation in compression and tension. Sections III B 3 characterizes the material's thermal properties and reports the pressure-boosted AlIn_2As_2 structural phase transition temperature. Sections III B 4 reveals the phenomenon of zero group velocity (ZGV) induced by softening of phonon modes under pressure and the enhancement of thermal conductivity. Section IV provides a summary of this study. Appendix A presents the details of the remaining auxiliary calculation methods. Appendix A 1 gives information on the calculation of phonon dispersion spectra and thermodynamic parameters. Appendix A 2 presents the relevant parameters for the characterization of mechanical properties, including equations for the calculation of elastic modulus, mechanical stability criterion, crystal anisotropy, calculation of chemical bonding information, and hardness analysis. In the Appendix B, we present and discuss other complementary results, such as the evolution of lattice parameters, symmetry transformation of point group, elastic modulus analysis, chemical bonding, toughness and brittleness, and hardness prediction. Supplemental Material (SM) [30] gives additional figures related to mechanical and thermal properties.

II. CALCULATION METHODS AND CRYSTAL STRUCTURES

First-principles calculations based on density functional theory (DFT) are performed in Vienna *ab initio* simulation package (VASP) [31,32] based on projected augmented wave (PAW) [33] and Perdew-Burke-Ernzerhof (PBE) type generalized gradient approximation (GGA) [34] exchange-correlation function. The valence wave functions are expanded on plane-wave basis with a 400 eV energy cutoff. In addition, the s semicore orbital of the A atoms are considered as a valence electron. Spin-orbit coupling (SOC) was considered in all our calculations. For ion relaxation, the absolute magnitude of the force on each atom is reduced to less than 0.02 eV/Å. For AlIn_2As_2 with three kinds of space groups [$P6_3/mmc$ (No. 194), $R\bar{3}m$ (No. 166), and $P2/m$ (No. 10)], the Γ -centered Monkhorst-Pack k -point mesh is considered as $11 \times 11 \times 3$, $21 \times 21 \times 3$, and $5 \times 13 \times 4$, respectively.

According to report [21], the structures of CaIn_2As_2 and SrIn_2As_2 are crystallized as EuIn_2P_2 type with $P6_3/mmc$ phase, whereas BaIn_2As_2 is crystallized in the monoclinic EuGa_2P_2 structure type with $P2/m$ phase. We further found that the hexagonal structure with $R\bar{3}m$ phase may also exist in these materials. To understand this structural phase difference, pressure was used to systematically study AlIn_2As_2 ($A = \text{Ca}, \text{Sr}, \text{Ba}$) for three space groups.

Three structures are obtained by arranging octahedral structural units and In atoms in different ways. For $P6_3/mmc$ phase, A atom occupies the $2a$ position while In and As occupy the $4f$ position. The adjacent octahedral lattices of the $P6_3/mmc$ phase, which was labeled as O_1 , form a mirror-symmetric alternating stack between them in the z direction, and two In atomic layers are inserted in between, also mirror symmetric about the z direction. The right part of Fig. 1(a) gives a schematic diagram of the O_1 octahedral lattice, with the isosceles triangular planes marked in cyan color and the equilateral triangular planes depicted in red color. The Ba-As octahedral of both $P6_3/mmc$ and $R\bar{3}m$ phases are connected by the edges in cyan color in the schematic diagram. For $R\bar{3}m$ phase, A atom occupies the $3a$ position while In and As occupy the $6c$ position. The In atomic layers of the $R\bar{3}m$ phase are arranged similarly to $P6_3/mmc$ phase, while the octahedral structural units are arranged along a translational stacking in the T direction as shown by the red arrow in Fig. 1(b).

However, the structure with $P2/m$ space group with low symmetry is quite different from the previous two. The Ba-As octahedral layer of the $P2/m$ phase consists of a combination of two types of octahedral lattices, O_2 and O_3 , as shown in the right part of Fig. 1(c). O_2 consists of four isosceles triangles (marked in purple and yellow colors) and four irregular triangles. O_3 consists of four isosceles triangles with different edge lengths, indicated by different colors. Compared to O_1 and O_2 , the top view of O_3 has a clear shift of the As and A atoms. As shown in the shaded background part of the octahedral schematic in Fig. 1(c), the [101] orientation, one end of the O_3 octahedral lattice is connected to the yellow-colored edge labeled in O_2 through the yellow-colored edge, which is noted as O_2 - O_3 . And the other end of O_3 is coedged with the yellow-colored part of O_2 through the labeled green

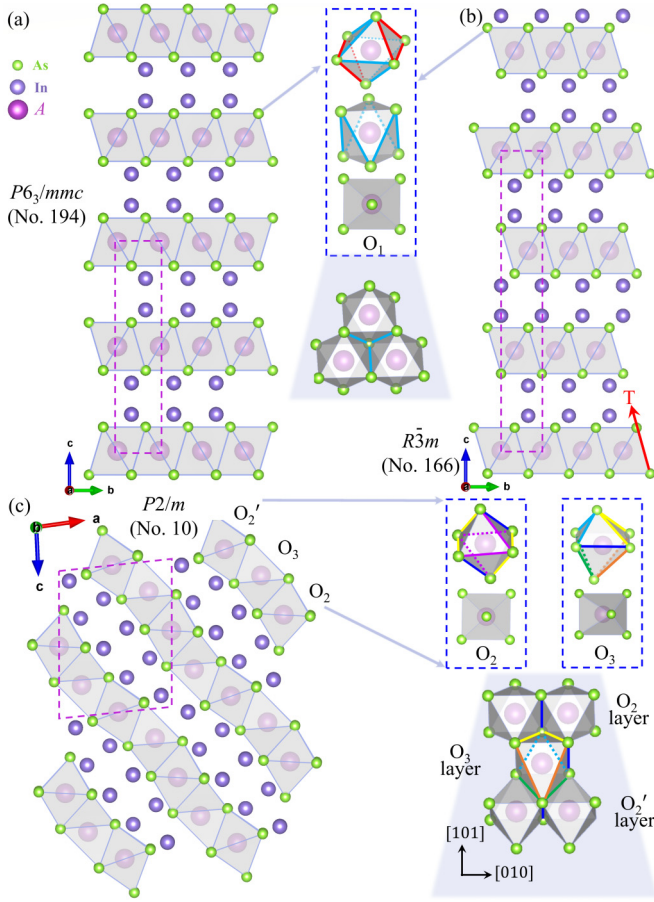


FIG. 1. AlIn_2As_2 crystal structure with (a) $P6_3/mmc$, (b) $R\bar{3}m$, and (c) $P2/m$ space groups. A schematic diagram of the A-As octahedra forming the corresponding structures is also included.

color edge, which is noted as $O_2'-O_3$. Note in particular that although in the $[101]$ orientation both ends of O_3 are connected to the yellow-colored part of O_2 by coedges, their edge lengths are not equal and depend on the lengths of the yellow-colored and green-colored parts of O_3 , respectively. In the $[010]$ orientation, both O_2 and O_2' layers are spliced via the blue-colored coedge in the O_2 octahedral lattice, and the O_3 layer is also connected by the blue-colored edge of the O_2 octahedral lattice.

Figures 1(a), 1(b), and 1(c) show the structures of AlIn_2As_2 , which belongs to the space group $P6_3/mmc$, $R\bar{3}m$, and $P2/m$, respectively. The hexagonal structure of the $P6_3/mmc$ and $R\bar{3}m$ phases is composed of alternating $[\text{In}_2\text{As}_2]^{2-}$ layers separated by a slab of A^{2+} cations. The structure of $P2/m$ phase is also layered and it is composed of different types of polyanions $[\text{In}_2\text{As}_2]^{2-}$ units and A^{2+} cations. They all exist as structural units formed by octahedral with A atoms at the center and As atoms occupying the vertices. The specific structural distinctions are described accordingly in the SM [30]. In short, the valence electron numbers of all three compounds follow the Zintl-Klemm formalism and all elements achieve closed-shell electronic configurations. Lattice parameters reported experimentally are $a = 4.148$ (4.222) Å and $c = 17.726$ (18.110) Å for CaIn_2As_2 (SrIn_2As_2) with

TABLE I. Summary table of AlIn_2As_2 different structural phases dependent on pressure. (+) indicates a relatively stable structural phase and (-) indicates a relatively unstable structural phase. NPMP and HPP are abbreviations for negative-pressure mixed phase and high-pressure phase, respectively.

Space group	CaIn_2As_2	SrIn_2As_2	BaIn_2As_2
$P6_3/mmc$	≤ 10 GPa(+)	< 6 GPa (+)	< 0 GPa (NPMP)
$R\bar{3}m$	(-)	< 6 GPa(+)	< 0 GPa (NPMP)
$P2/m$	> 10 GPa(+)	≥ 6 GPa(+)	< 0 GPa (NPMP), ≥ 0 GPa (HPP)

$P6_3/mmc$ space group and $a = 10.275$ Å, $b = 4.301$ Å, $c = 13.332$ Å, and $\beta = 95.569$ degree for $P2/m$ space group.

The symmetry generators of $P6_3/mmc$ contain identity operation \mathcal{E} , inversion symmetry \mathcal{I} , twofold screw rotation axis $\mathcal{G}_{2z} = \{C_{2z}|00\frac{1}{2}\}$, threefold rotation axis C_{3z} , and the combined rotation axis $C_{2(110)}$. Slightly different with $P6_3/mmc$, $R\bar{3}m$ space group with a hexagonal lattice lacks the \mathcal{G}_{2z} operation but has an additional lattice translation operation $T = \{x + \frac{2}{3}, y + \frac{1}{3}, z + \frac{1}{3}\}$. While the $P2/m$ has lower symmetry generators that named twofold screw rotation axis C_{2y} (unique axis b), identity operation \mathcal{E} , and inversion symmetry \mathcal{I} . These basic operations will generate a total of 24, 36 (12×3 sets), and four symmetric operations for the $P6_3/mmc$, $R\bar{3}m$, and $P2/m$ space groups, respectively.

III. RESULTS AND DISCUSSION

A. Structural stability and structural phase transition

1. Dependence of enthalpy on pressure in different structural phases

Enthalpy is an important state parameter in thermodynamics that characterizes the energy of a material system. It is equal to the sum of the product of internal energy and pressure and volume and can be expressed as $H = U + pV$, where U is the internal energy of the system, p is the pressure of the system, and V is the volume.

Thus, we first investigated the enthalpy of different structural phases of AlIn_2As_2 under the controlling of pressure [see Figs. 2(a)–2(c)]. In different AlIn_2As_2 systems, the enthalpy difference (ΔH) between the two hexagonal phases ($P6_3/mmc$ and $R\bar{3}m$) under pressure relative to the monoclinic phase ($P2/m$) has different trends. Since $P6_3/mmc$ and $R\bar{3}m$ have similar crystal structures and symmetry operations, their pressure-dependent enthalpy evolution trends behave approximately the same [see green and red curves in Figs. 2(a)–2(c)]. The purple dashed lines in Figs. 2(a)–2(c) mark the approximate values of the transition pressure of the structural phase transition, with the left side of the transition point indicating a more likely formation of the hexagonal phase ($P6_3/mmc$ or $R\bar{3}m$), while the right region indicates a more likely formation of the monoclinic phase with $P2/m$ space group. For CaIn_2As_2 , SrIn_2As_2 , and BaIn_2As_2 systems, the phase transition points move toward low pressure, respectively, and BaIn_2As_2 in particular basically tends to exhibit a $P2/m$ phase, which is consistent with the experimentally reported results [21]. As summarized in Table I, unlike

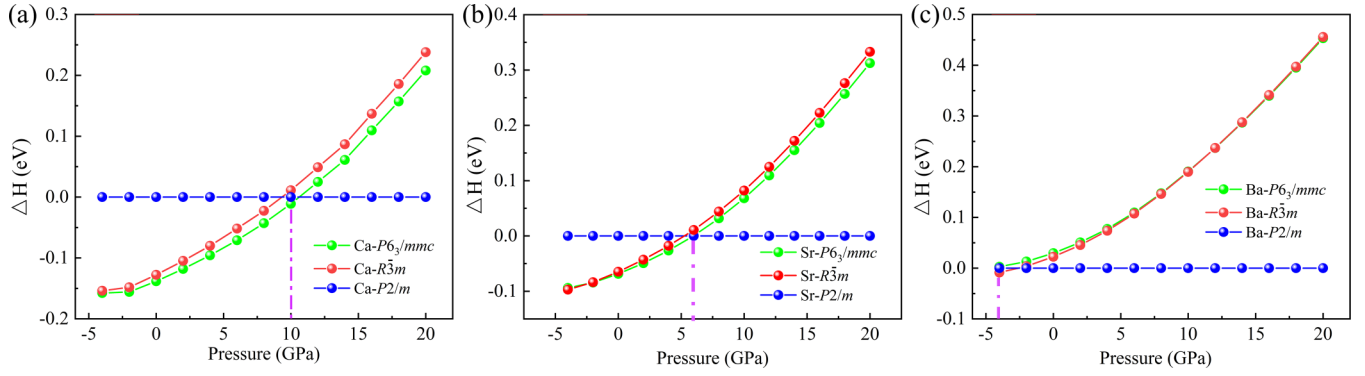


FIG. 2. The enthalpy differences of the three structured phases of (a) CaIn_2As_2 , (b) SrIn_2As_2 , and (c) BaIn_2As_2 , with the energy of the $P2/m$ phase as the reference value.

BaIn_2As_2 , CaIn_2As_2 and SrIn_2As_2 tend to form hexagonal structured phases at pressures below 10 GPa and 6 GPa, which explains the experimental conclusion that CaIn_2As_2 and SrIn_2As_2 have a different space group structure than BaIn_2As_2 . For BaIn_2As_2 , a negative-pressure mixed phase (NPMP) with similar energy of the three structural phases will appear at tension stress (negative pressure values), while a $P2/m$ high-pressure phase (HPP) will formed at compressive stress (positive pressure values). Thus, we achieved a series of pressure-dependent structural phase transitions for the AlIn_2As_2 systems. The change in hardness of the hexagonal and monoclinic phases under pressure is predicted from Table II. See Appendix B 3 d for details.

2. Phonon dispersion spectrum analysis

To better illustrate the structural phase transition of AlIn_2As_2 , we further compare the structural stability of AlIn_2As_2 under pressure for different space groups by phonon dispersion spectroscopy calculations. As shown in Fig. 3, the phonon and projected density of states (PDOS) calculations show that the AlIn_2As_2 systems of the $P6_3/mmc$ space group are all stable structures at both atmospheric pressure and zero-bandgap pressure. The pressure values at which the zero bandgap appears in the induced system have been reported in previous study and are 3 GPa, 6.637 GPa, and 10.555 GPa for CaIn_2As_2 , SrIn_2As_2 , and BaIn_2As_2 , respectively [20]. And we have shown that the system will undergo a nontrivial to trivial topological transitions at these pressure critical values [20]. The lattice waves of the acoustic and optical branches are distinguished in the phonon spectrum by yellow and green curves, respectively. From Figs. 3(a)–3(l), the acoustic branching lattice waves of the systems with space group

$P6_3/mmc$ have complete degeneracy in the A-L, L-H, and H-A high-symmetry paths. The BaIn_2As_2 of the $R\bar{3}m$ and $P2/m$ space groups do not have fully phonon dispersion degeneracy in any of the Brillouin zone paths we have considered (see Fig. S11 within the SM [30]).

From the PDOS images in Fig. 3, it can be found that the low-frequency parts of CaIn_2As_2 and SrIn_2As_2 are mainly composed of the phonon dispersion of the In element, while the contribution of the Ba element in the BaIn_2As_2 systems are more prominent in the low-frequency phonon dispersion, as the red arrow shown in Figs. 3(j) and 3(l). Two relatively flat high-frequency phonon dispersions consisting of As and In elements exist for the SrIn_2As_2 and BaIn_2As_2 systems, corresponding to the local peaks in the PDOS diagrams. Similarly, there is a local peak in the 2–3 THz region consisting mainly of A elements. Compared to the atmospheric pressure system, the phonon spectrum of the zero-bandgap pressure system has a broader distribution and spreads to the high-frequency region (see Fig. 3). For BaIn_2As_2 structures with different space groups, all have stable phonon characteristics at atmospheric pressure have shown in Figs. 3 and S11 within the SM [30]. As shown in Fig. S11(b) within the SM [30], the acoustic branching lattice wave has a slight imaginary frequency near Γ , indicating that the structure with $R\bar{3}m$ space group is less stable under the action of 14 GPa than at atmospheric pressure. From Fig. S11(d) within the SM [30], the structure with $P2/m$ space group can still exist stably when 14 GPa is applied. Thus, for the BaIn_2As_2 system, as shown in the enlarged plots in Figs. 3(k) and S11(b) and S11(d) within the SM [30], it is shown that the hexagonal phase is not stable at high pressure, while the monoclinic phase with the $P2/m$ space group is stable. The phonon spectrum calculation verifies our result that BaIn_2As_2 has a NPMP and

TABLE II. Hardness prediction results for different structural phases dependent on the band gap.

Type of material	General	Cubic	Hexagonal	Orthorhombic	Rhombohedral
Insulator ($E_g > 2$ eV)	H_2	H_2	H_{1b}	H_2	H_2
Semiconductor ($0 < E_g < 2$ eV)	H_5	H_5	H_{1b}, H_3		H_2
Metal ($E_g = 0$)	H_4	H_{1a}	H_4	H4	H_4

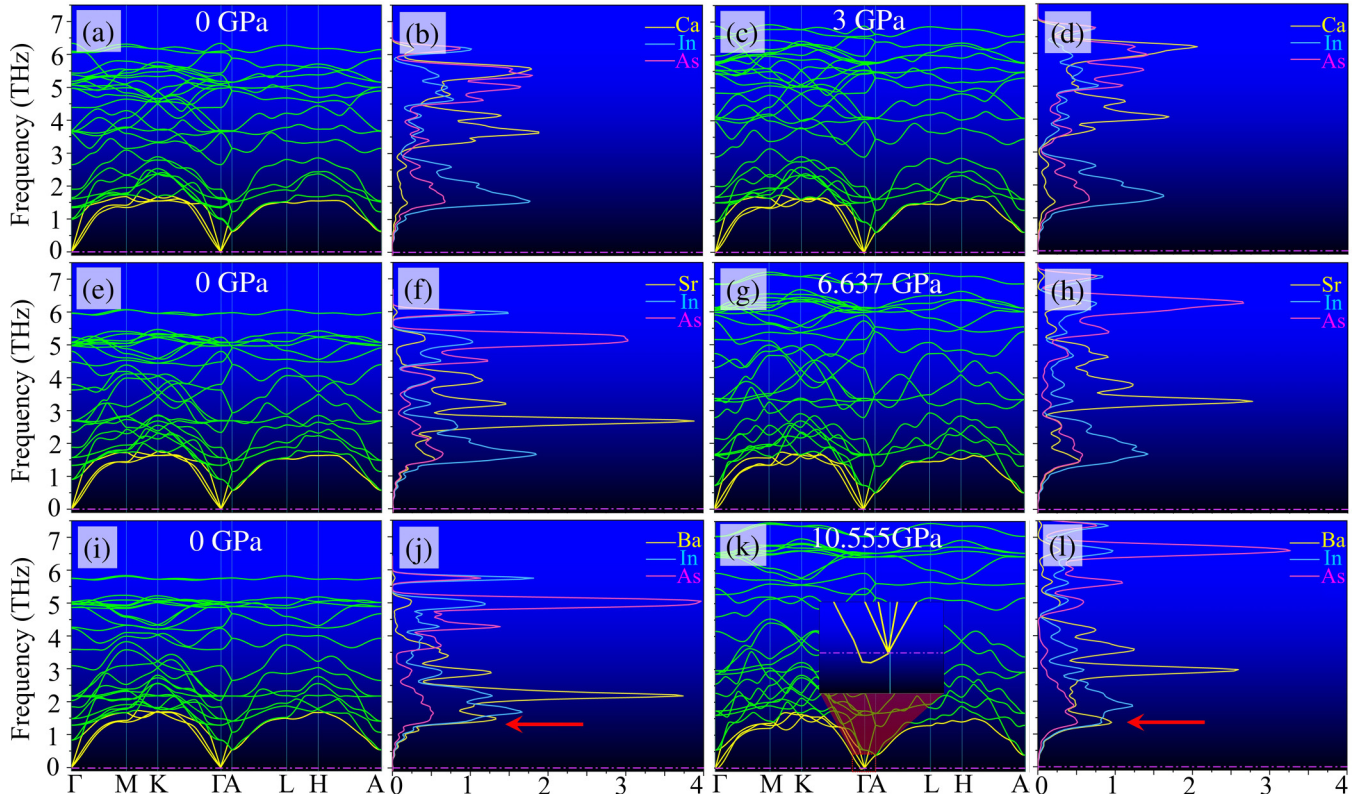


FIG. 3. Phonon dispersion and local phonon density of states combinations for (a)–(d) CaIn_2As_2 , (e)–(h) SrIn_2As_2 , and (i)–(l) BaIn_2As_2 with $P6_3/mmc$ space group at atmospheric pressure and zero-bandgap pressure, respectively.

a HPP ($P2/m$ space group), as considered from the energy comparison. In a word, our high-pressure calculations realized the structural phase transition of AlIn_2As_2 bulk materials. And we further reveal that they are pressure-tunable and can exist stably in a specific pressure range, which is beneficial for the experimentally study.

3. Symmetry transformation of point group

Here, we perform a detailed symmetry theory analysis of the structural phase transition. The structure of the fully relaxed $P6_3/mmc$ space group cannot be directly establish a symmetry transition with the $P2/m$. But we note that the $P6_3/mmc$ structure belongs to the same hexagonal crystal system as $R\bar{3}m$. Their lattice structures are very similar and only a simple lattice perturbation is required to achieve the structural transformation. Then, the $R\bar{3}m$ phase structure can be transformed into the $P2/m$ phase through a series of symmetry transformations, as shown in Fig. 4(d). To understand more deeply the evolutionary mechanism behind the structural phase transition under pressure, we calculate the Raman and infrared-Raman (IR) activity for these two space groups [see Fig. 4(e) and Table III]. The phonon modes at Γ point can be decomposed into different irreducible representations, and the correspondence between the irreducible representations of the two phases is shown in Table IV.

We utilize the overall transformation matrix T [Eq. (B1)] to realize the structural phase transition from $R\bar{3}m$ to $P2/m$ [from Figs. 4(a) to 4(b)], and then the lattice perturbation to obtain Fig. 4(c). T can be obtained by $GS \times EAN \times EEN$,

and $LC = GS \times EAN$, where the transformation matrices group-subgroup, element of the affine normalizers, lattice compatible, and element of the euclidean normalizers are represented by GS , EAN , LC , and EEN , respectively. As shown in Table IV, the irreducible representations of the two point groups at Γ have a clear correspondence. It is worth noting that A_{1u} and A_{2g} of $R\bar{3}m$ are both Raman inactive and IR inactive [see Fig. 4(e)]. On the other hand, determining exactly which atoms contribute to these activities will be one of the most important factors influencing the trend of the structural phase transition. As shown in Table III, the Raman activity A_g (B_g) of the $P2/m$ phase is mainly in the m site symmetry

TABLE III. Wyckoff positions (WP), site symmetry group (SSG), and mechanical representation of every atoms in $P2/m$ and $R\bar{3}m$ space groups.

SG	Atoms	Coordinates	WP	SSG	Mechanical rep.
$P2/m$	A	(1/2,0,0)	1d	2/m	$A_u + 2B_u$
		(0,0,1/2)	1c	2/m	
	In	(x,1/2,z)	2n	m	$2A_g + A_u + B_g + 2B_u$
		(x,0,z)	2m	m	
	As	(x,1/2,z)	2n	m	
		(x,0,z)	2m	m	
$R\bar{3}m$	A	(0,0,0)	3m	-3m	$A_{2u} + E_u$
	In	(0,0,z)	6m	3m	$A_{1g} + A_{2u} + E_u + E_g$
	As	(0,0,z)	6m	3m	

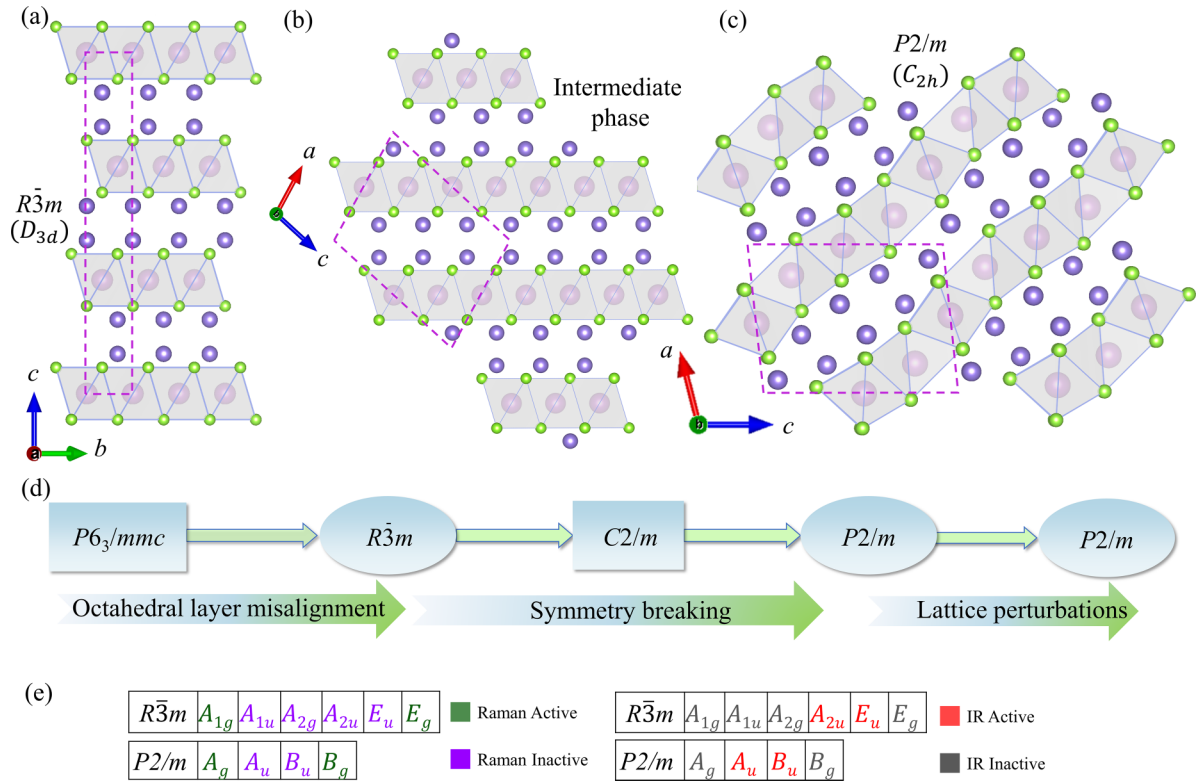


FIG. 4. [(a)–(c)] Crystal structure of the $R\bar{3}m$ phase, the crystal structure of the intermediate phase $P2/m$ obtained by a transformation matrix, and our calculated crystal structure of the monoclinic phase ($P2/m$). (d) Schematic diagram of the transition from hexagonal to monoclinic phase with the reason for the structural phase transition labeled below. (e) Raman and infrared Raman (IR) activity characterization of $R\bar{3}m$ and $P2/m$ irreducible representation.

group, which can be contributed by In, As, or A atoms at the $2n$ Wyckoff site. And the IR-active A_u (B_u) can be contributed by any site of atoms. For the $R\bar{3}m$ phase, the Raman activities A_{1g} and E_g are contributed by In, As atoms only, while the IR activities A_{2u} and E_u can be contributed by any kind of atoms as well.

Furthermore, we note the existence of an intermediate phase $C2/m$ for this phase change process. A total of six transformation matrix channels with indices $[3\ 2\ 2]$ are available for the conversion of the symmetric operation between these two phases, as shown in Eq. (B2). The result obtained by their structure relations of group $G = R\bar{3}m$ and subgroup $H = P2/m$ belongs to a class with the chain $R\bar{3}m \rightarrow C2/m \rightarrow P2/m \rightarrow P2/m$ and index 12. To change the basis of the group general positions is used the transformation matrices $P = (P, p)$ are shown in Eq. (B2). The linear part P_i of the transformation $P = (P, p)$ implies the change of basis vectors, and the column p describes the origin shift $O' = O + p$. And the symmetric operations of group $R\bar{3}m$ (see Table V) and subgroup $P2/m$ (see Table VI) can be fully correlated by

$R_{P2/m} = Q \times R_{R\bar{3}m} \times P$, where Q is the inverse transformation of P .

According to this relationship, the identity (ε) and inverse (I) symmetry operations with low symmetry can naturally be represented by the corresponding ones with high symmetry. However, C_{2y} and IC_{2y} in the $P2/m$ phase can have different $R\bar{3}m$ transition symmetry operations, which are C_{2x} , IC_{2x} (P_1 and P_2) or C_{2y} , IC_{2y} (P_3 and P_4) or C_{2xy} , IC_{2xy} (P_5 and P_6), respectively. For example, the following Eq. (B2) gives the C_{2y} symmetric operation of the $P2/m$ phase based on the P_1 transformation matrix using the C_{2x} symmetric operation of the $R\bar{3}m$ phase.

In conclusion, we achieved the structural phase transition of the $AlIn_2As_2$ system from the hexagonal phase ($P6_3/mmc$ and $R\bar{3}m$) to the monoclinic phase ($P2/m$) from the symmetry operation point of view. As summarized by the schematic diagram of the structural phase transition in Fig. 4(d), the $P6_3/mmc$ phase can be transformed into the $R\bar{3}m$ phase after a simple octahedral layer dislocation. Then the intermediate phase $C2/m$ and the regular $P2/m$ [Fig. 4(b)] are obtained

TABLE IV. The irreducible representation of the transformation relation between the D_{3d} point group and the C_{2h} point group at the Γ -high symmetry point.

k vector	$\Gamma (0, 0, 0)$						
Relations between the irreps	$D_{3d} (-3m)$	A_{1g}	A_{1u}	A_{2g}	A_{2u}	E_g	E_u
	$C_{2h} (2/m)$	A_g	A_u	B_g	B_u	A_g+B_g	A_u+B_u

TABLE V. Symmetry operations of $R\bar{3}m$ space group.

SO	Seitz symbols	(x,y,z) form	Matrix form
ε	$\{1 0\}$	x,y,z	$\begin{pmatrix} 1 & 0 & 0 \\ 0 & 1 & 0 \\ 0 & 0 & 1 \end{pmatrix}$
I	$\{-1 0\}$	$-x,-y,-z$	$\begin{pmatrix} -1 & 0 & 0 \\ 0 & -1 & 0 \\ 0 & 0 & -1 \end{pmatrix}$
C_{2x}	$\{2_{100} 0\}$	$x-y,-y,-z$	$\begin{pmatrix} 1 & -1 & 0 \\ 0 & -1 & 0 \\ 0 & 0 & -1 \end{pmatrix}$
IC_{2x}	$\{m_{100} 0\}$	$-x+y,y,z$	$\begin{pmatrix} -1 & 1 & 0 \\ 0 & 1 & 0 \\ 0 & 0 & 1 \end{pmatrix}$
C_{2y}	$\{2_{010} 0\}$	$-x,-x+y,-z$	$\begin{pmatrix} -1 & 0 & 0 \\ -1 & 1 & 0 \\ 0 & 0 & -1 \end{pmatrix}$
IC_{2y}	$\{m_{010} 0\}$	$x,x-y,z$	$\begin{pmatrix} 1 & 0 & 0 \\ 1 & -1 & 0 \\ 0 & 0 & 1 \end{pmatrix}$
C_{2xy}	$\{2_{110} 0\}$	$y,x,-z$	$\begin{pmatrix} 0 & 1 & 0 \\ 1 & 0 & 0 \\ 0 & 0 & -1 \end{pmatrix}$
IC_{2xy}	$\{m_{110} 0\}$	$-y,-x,z$	$\begin{pmatrix} 0 & -1 & 0 \\ -1 & 0 & 0 \\ 0 & 0 & 1 \end{pmatrix}$

after the symmetry-breaking by the symmetry-operated transformation. Finally, a simple lattice perturbation is required to induce the transformation of the well-aligned $P2/m$ phase into the actual $P2/m$ structure we calculated [Fig. 4(c)],

$$\begin{aligned}
 QRP &= \begin{pmatrix} 0 & 1/2 & 1 \\ 1 & -1/2 & 0 \\ 0 & 3/4 & 0 \end{pmatrix} \begin{pmatrix} 1 & -1 & 0 \\ 0 & -1 & 0 \\ 0 & 0 & -1 \end{pmatrix} \begin{pmatrix} 0 & 1 & 2/3 \\ 0 & 0 & 4/3 \\ 1 & 0 & -2/3 \end{pmatrix} \\
 &= \begin{pmatrix} -1 & 0 & 0 \\ 0 & 1 & 0 \\ 0 & 0 & -1 \end{pmatrix} = C_{2y}(P2/m). \quad (1)
 \end{aligned}$$

TABLE VI. Symmetry operations of $P2/m$ space group.

SO	Seitz symbols	(x,y,z) form	Matrix form
ε	$\{1 0\}$	x,y,z	$\begin{pmatrix} 1 & 0 & 0 \\ 0 & 1 & 0 \\ 0 & 0 & 1 \end{pmatrix}$
C_{2y}	$\{2_{010} 0\}$	$-x,y,-z$	$\begin{pmatrix} -1 & 0 & 0 \\ 0 & 1 & 0 \\ 0 & 0 & -1 \end{pmatrix}$
I	$\{-1 0\}$	$-x,-y,-z$	$\begin{pmatrix} -1 & 0 & 0 \\ 0 & -1 & 0 \\ 0 & 0 & -1 \end{pmatrix}$
IC_{2y}	$\{m_{010} 0\}$	$x,-y,z$	$\begin{pmatrix} 1 & 0 & 0 \\ 0 & -1 & 0 \\ 0 & 0 & 1 \end{pmatrix}$

B. Performance change after structural phase transition under pressure

1. Regulation of crystal anisotropy

Based on the elastic constants analyzed in Appendix B 3 a, we can get the following results. First, we predict that the hexagonal phase $BaIn_2As_2$ is more compressible in the ab plane, and the octahedral layer in Fig. 1(a) is more susceptible to phase transitions in the ab plane. In contrast, the structural phase transitions of $CaIn_2As_2$ and $SrIn_2As_2$ are in the c direction. This difference explains that experimentally $BaIn_2As_2$ has different structural phases from $CaIn_2As_2$ or $SrIn_2As_2$. The monoclinic phase of $AlIn_2As_2$ has a structural phase transition in the a direction, which is manifested by weaker bonding in the a axis and relatively easy stripping in that direction. Immediately after that, we find that the bulk modulus B , shear modulus G , and Young's modulus E of the two-phase structures will be effectively regulated by pressure and show different trends (see Table VII).

According to the Appendix B 3 b, we have described and analyzed the significance of the various moduli of elasticity and the trend of their evolution under pressure. The three-dimensional (3D) figures of various elastic moduli (G , E , linear compression LC) in the SM show that the anisotropic properties of the different structural phases of $AlIn_2As_2$ differ significantly. Various elastic moduli of hexagonal phase ($P6_3/mmc$) $AlIn_2As_2$ under no pressure tend to be crystal isotropic, especially for $BaIn_2As_2$ (see Fig. S1 within the SM [30]). As shown in the first two rows of Fig. S2 within the SM [30], $CaIn_2As_2$ and $SrIn_2As_2$ remain isotropic in their elastic moduli due to too little pressure. However, at 10.555 GPa, the G , E , and ν of the $BaIn_2As_2$ system shift to anisotropy, and the LC tends to remain isotropic (see the third row of Fig. S2 within the SM [30]). In sharp contrast to the hexagonal phase, the monoclinic ($P2/m$) $AlIn_2As_2$ systems exhibit significant crystal anisotropy under no pressure (see Figs. S3–S5 within the SM [30]). Moreover, the pressure will further enhance the anisotropy of the individual elastic moduli of the monoclinic phase $AlIn_2As_2$ system. 2D projections of the pressure-regulated G , E , LC , and ν associated with $CaIn_2As_2$, $SrIn_2As_2$, and $BaIn_2As_2$ are presented in the SM as Figs. S6–S10 [30]. For a detailed analysis of the anisotropy of these mechanical parameters projected in the xy , yz , and xz directions, see Appendix B 3 c.

We further compared the bulk anisotropy and plane anisotropy coefficients for each elastic modulus of $AlIn_2As_2$ under pressure (see Fig. 5). The anisotropy coefficients of the hexagonal phase ($P6_3/mmc$) mostly exhibit isotropic features and are distributed around the red dashed line in Fig. 5. For G and E of the hexagonal phase, the pressure will somehow enhance their degree of anisotropy. In contrast, the degree of anisotropy of LC and ν shows robustness to the pressure. G in hexagonal phase $AlIn_2As_2$ at all pressures and monoclinic phase $AlIn_2As_2$ at 0 GPa exhibit equal bulk and plane anisotropy coefficients [see Fig. 5(a)]. The pressure will break the equilibrium of equal bulk and plane anisotropy coefficients for the monoclinic phase, and the enhancement of the bulk anisotropy mainly comes from the two-plane anisotropy enhancement of xy and xz . In contrast, the G anisotropy of the yz plane is robust for pressure, which does not become

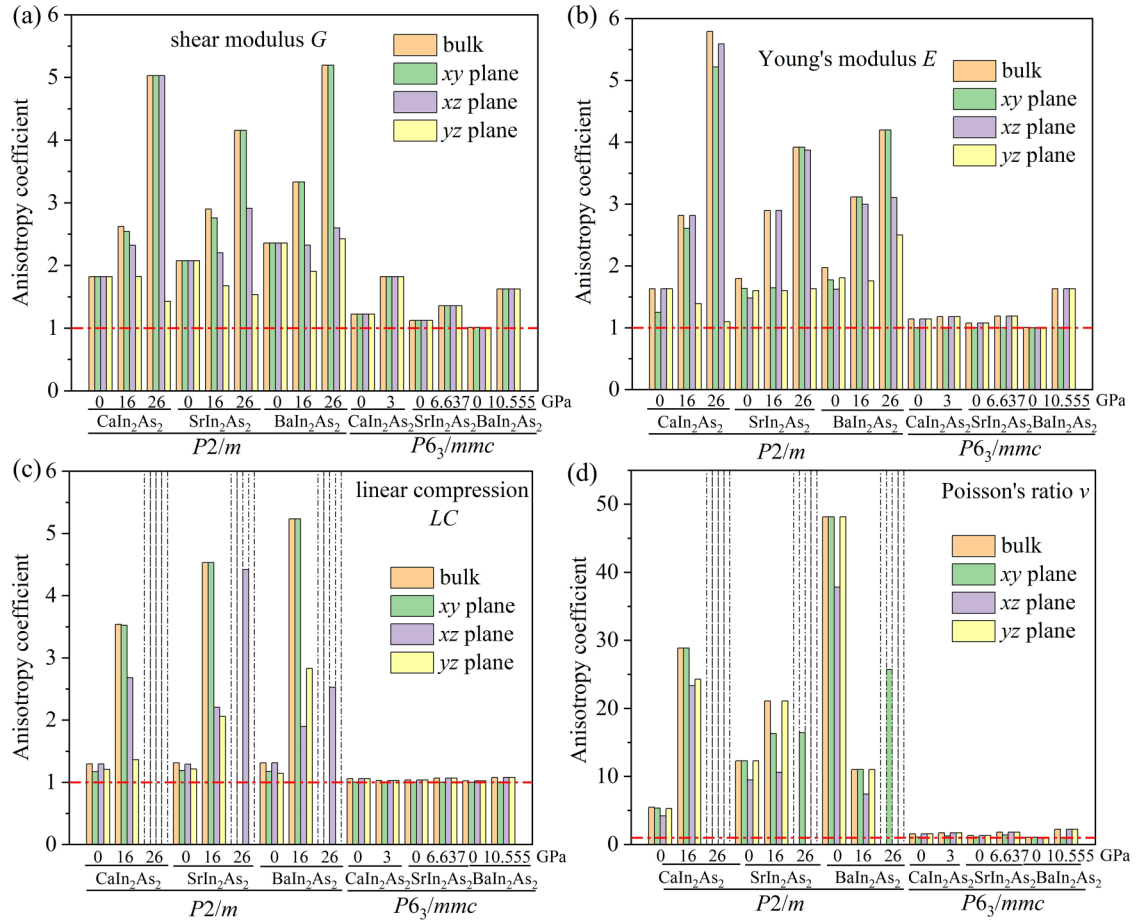


FIG. 5. Bulk anisotropy coefficients and plane anisotropy coefficients for hexagonal phase and monoclinic relative to (a) G , (b) E , (c) LC , (d) ν under pressure. The red dashed line indicates the anisotropy coefficient $A = 1$, representing the complete isotropy. The dashed column indicates infinity anisotropy coefficients, which means that the minimum value of the modulus of elasticity is 0 or negative.

significantly more extensive due to pressure, as shown by the yellow rectangle of the $P2/m$ phase in Fig. 5(a). Similarly, the yz plane anisotropy of Young's modulus E and linear compression LC in the monoclinic phase $A\text{In}_2\text{As}_2$ do not become much larger under pressure modulation. In contrast, the xy or xz plane E and LC anisotropies are an essential reason for the significant increase in the anisotropy of the bulk E and bulk LC [see Figs. 5(b) and 5(c)]. Of interest is the monoclinic phase system where LC and Poisson's ratio ν appears to have a minimum value of 0 or even negative at 26 GPa, resulting in an anisotropy of infinity [see the dashed hollow rectangles in Figs. 5(c) and 5(d)]. Although the bulk anisotropy coefficients tend to infinity, there are finite anisotropy coefficients (non-infinity) for SrIn_2As_2 (BaIn_2As_2) for LC and ν in the xz plane and xy plane, respectively. Moreover, they both undergo a dramatic change in anisotropy under pressure modulation, with the same pattern as the 2D analysis above. Their anisotropy can be described by the two anisotropy constants A_U and A_L in Table VIII, which can be calculated by Eqs. (A15) and (A16). The values of A_U and A_L illustrate that BaIn_2As_2 in the hexagonal phase is completely isotropic at 0 GPa and that the pressure can substantially enhance the system anisotropy. In addition, the monoclinic phase's anisotropy is stronger than the hexagonal phase's. Calculating the anisotropy constants leads to an assertion consistent with the previous discussion.

2. Realization of negative Poisson's ratio material

Poisson's ratio is the opposite of transverse strain to axial strain when a material is tensile or compressive in a particular direction. NPR materials, also known as auxetic materials, have several excellent properties because of their unique mechanical structure, including superior fracture resistance, shear resistance, sound and energy absorption, dent resistance, and surface isotropy [35–37]. Although NPR is allowed by thermodynamics, this property is rare in crystalline solids [38]. NPR is mainly studied in 2D materials and structures, and it is crucial to design a 3D multilevel system that can exhibit NPR under deformation [39]. It is difficult to find materials that can show a negative Poisson ratio under both pressure and tension, and it is even rarer to find materials or structures that can have the same NPR performance under tension and compression stresses [39].

Using pressure modulation, we observe a NPR phenomenon in $A\text{In}_2\text{As}_2$ with low symmetry $P2/m$ phase. In the case of CaIn_2As_2 , for example, the system exhibits a generally NPR behavior in the absence of pressure or at low compressive stresses [see Figs. 6(b) and 6(c)]. At both tensile pressure of -4 GPa [see Fig. 6(a)] and compressive pressure of 26 GPa [see Fig. 6(d)], the material rarely exhibits NPR property. We predict that this NPR material can be widely used for many

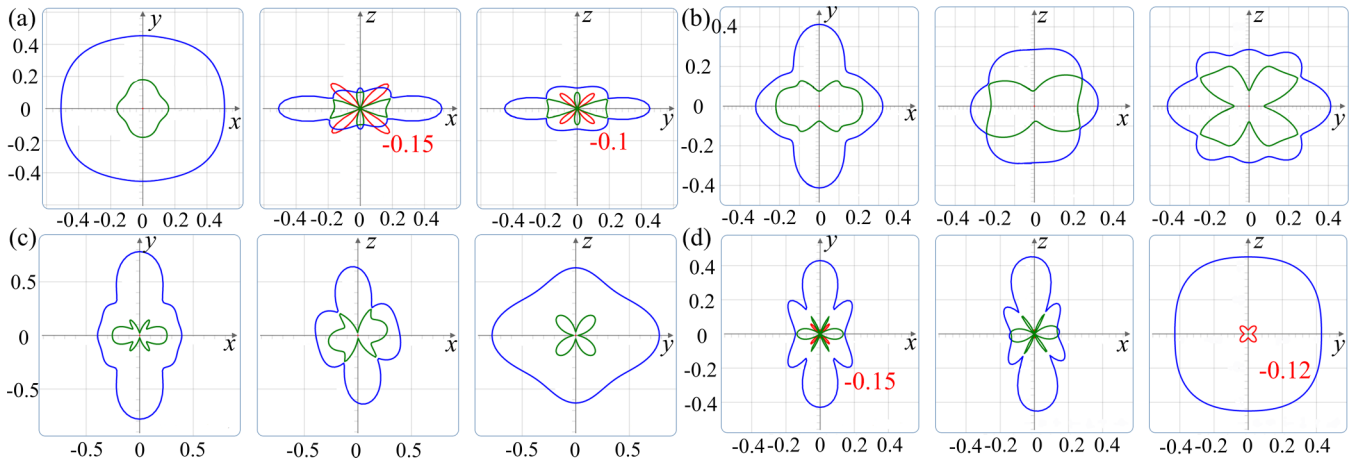


FIG. 6. Poisson's ratio (ν) of CaIn_2As_2 in xy , xz , and yz planes. (a)–(d) monoclinic phase under -4 GPa, 0 GPa, 16 GPa, and 26 GPa pressures.

applications in medical devices, cushioning and protective equipment, intelligent sensors, and defense industries.

3. Thermal properties analysis and enhance in phase transition temperature

Experimentally synthesized BaIn_2As_2 ($P2/m$) has different structural phases from CaIn_2As_2 and SrIn_2As_2 ($P6_3/mmc$). The above first-principles calculations based on absolute zero ($T = 0$ K) conditions give detailed results of the structural phase transition. However, the thermodynamic physical picture of the structural phases at high temperatures is still blurred. Here, we calculate the dependence of thermodynamic parameters on temperature between the hexagonal phase ($P6_3/mmc$) and the low-symmetry monoclinic phase ($P2/m$). The specific heat at constant volume C_V , the vibrational entropy $S_{\text{vib}}(T)$, the internal energy $U_{\text{vib}}(T)$, and the Helmholtz free energy $F(T)$ of individual harmonic oscillator and its difference $\Delta F_{P2/m-P6_3/mmc}(T)$ between two phases are given as Eqs. (A1)–(A5).

To investigate the mechanism of the response of the above-mentioned thermal parameters to temperature under pressure, we compared the thermodynamic curves of the two phases $P6_3/mmc$ and $P2/m$ under pressure, as shown in Figs. S13 and S14 within the SM [30]. As the pressure increases, both phases show an increase in free energy F (red curve), a decrease in entropy S (blue curve), and a convergence of the heat capacity C_V to a constant (green curve). As shown by the arrows in the enlarged diagram in the right column of Figs. S13 and S14 within the SM [30], the intersection of heat capacity and entropy tends to move towards higher temperatures as the pressure increases, except for BaIn_2As_2 in the $P2/m$ phase. This exception may be due to lattice distortion inducing a large phonon dispersion spectrum of imaginary frequencies at Γ (shown in Fig. S12(i) within the SM [30]). The phonon frequencies of each system of the $P2/m$ space group corresponding to Fig. S12 within the SM [30] at the point Γ are shown in Fig. S20(a) within the SM [30]. It is easy to find that CaIn_2As_2 at 0 GPa, BaIn_2As_2 at 16 GPa, and AlIn_2As_2 at 26 GPa all have large imaginary frequencies. The acoustic and optical branches for each

frequency correspond to the irreducible representation and activity (Raman or IR) are compared in Table S1 within the SM [30]. Unlike other systems where the acoustic branch consists of $A_u + 2B_u$, the acoustic branch of CaIn_2As_2 has B_g involved in the absence of pressure, and the B_u IR activity is squeezed to the fourth branch (-0.95 cm^{-1}), leading to the dynamic instability of the system. With the application of pressure, the phonon dispersion spectrum expands and shifts toward high frequencies while CaIn_2As_2 opens a gap near 100 cm^{-1} .

As shown in Fig. S15(a) within the SM [30], the curve of entropy increase indicates that the vibrational entropy favors a monoclinic phase of AlIn_2As_2 over a hexagonal phase. The vibrational entropy difference ($\Delta S_{P2/m-P6_3/mmc}$) between the two phases increases rapidly at low temperatures (≤ 250 K), and then the trend moderates as temperature increases to 3000 K. To quantitatively analyze the vibrational entropy, we give the temperature-dependent characteristic curves of free energy difference including the vibrational entropy [shown in Fig. S15(b) within the SM [30]]. At low temperatures, the free energy difference between the monoclinic phase and the hexagonal phase is positive, implying that the hexagonal phase is relatively stable. When the temperature increases, the vibrational entropy prefers to stabilize the monoclinic phase, which ($-T\Delta S(T) < 0$) becomes large enough to compensate for the 0 K energy difference ($\Delta E > 0$), prompting the free energy difference to become negative ($\Delta F(T) < 0$) and the phase transition from the hexagonal phase to the monoclinic phase occurs. The transition temperatures are 160 K, 156 K, and 148 K for CaIn_2As_2 , SrIn_2As_2 , and BaIn_2As_2 , respectively. The hexagonal and monoclinic phases are low- and high-temperature phases, respectively, which is inconsistent with the experimentally reported high temperature where CaIn_2As_2 and SrIn_2As_2 are hexagonal and BaIn_2As_2 are monoclinic phases [21]. This discrepancy may be caused by defects or lattice distortions under high temperature. As shown in Fig. 7, pressure can effectively raise the structural phase transition temperature of AlIn_2As_2 beyond absolute zero (273 K). The phase transition temperature decreases with the increased ionicity of the A atoms at 0 and 16 GPa, which is related to the strength of the interatomic chemical bonds. In

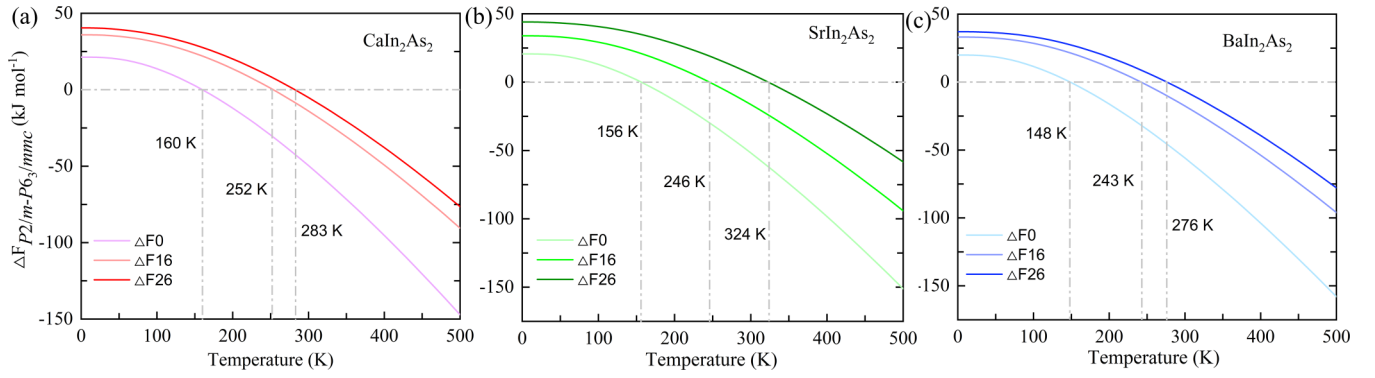


FIG. 7. Enlarged diagrams of the Helmholtz free energy difference for AlIn_2As_2 monoclinic and hexagonal phases under different pressures.

particular, the SrIn_2As_2 system will reach a higher temperature of 324 K at 26 GPa. Our results will provide critical pressure and temperature options for the experimental synthesis of AlIn_2As_2 in specific structural phases.

Although the heat capacity varies at low temperatures due to pressure (see green curves in Figs. S13 and S14 within the SM [30]), the heat capacity of the same phase eventually converges to the same constant independent of pressure and A elements, satisfying the Dulong-Petit limit at high temperatures. To observe the change of heat capacity at high temperatures more clearly, we found that the heat capacity of all systems near 1000 K did not reach Dulong-Petit limit (see Fig. S17 within the SM [30]). Except for CaIn_2As_2 ($P2/m$) under no pressure due to the existence of phonon dispersion at imaginary frequencies causing the heat capacity curve to fall below the 16 GPa case, all of them showed the phenomenon of lowering the high-temperature heat capacity worth after pressurization. When the temperature increases to 3000 K, CaIn_2As_2 with $P2/m$ phase at 0 GPa still cannot reach Dulong-Petit limit and has the situation of leveling off (see Fig. 8). The rest system of the absence of pressure can cross Dulong-Petit limit. However, as shown by the red dashed line in Fig. 8(b), applying a 16 GPa pressure can push the heat capacity curve beyond the Dulong-Petit limit.

4. Zero-group velocity behavior of phonon mode softening and Phonon thermal conductivity prediction

In order to study in depth the thermal conductivity properties and the sources of thermodynamic instability of the AlIn_2As_2 material at high pressures, we calculated phonon group velocities, as shown in Fig. 9. Figures 9(a)–9(c) demonstrate that the hexagonal phase ($P6_3/mmc$ space group) is both stable in the absence of pressure and at the induced zero-bandgap pressure. The pressure induces the group velocity towards lower and higher frequencies, behaving more divergent. In addition, both two phases of AlIn_2As_2 show a tendency for the group velocity to become larger in the medium and high-frequency regions with increasing pressure (see Fig. 9). Moreover, the low-frequency acoustic branch mainly contributes to the phonon thermal conductivity of all systems. However, compared to the hexagonal phase, the monoclinic phase of AlIn_2As_2 has larger group velocities in the low-frequency region, and the group velocities in the medium and high-frequency areas are all roughly distributed in the range of 2–3 km/s. The pressure drives a virtual frequency in the low-frequency region because of the appearance of softened phonon modes, which induces a ZGV [see Figs. 9(d)–9(f)].

The phonon thermal conductivity depends on the group velocity with the relation $\kappa = C v_g^2 \tau$, where τ is the average

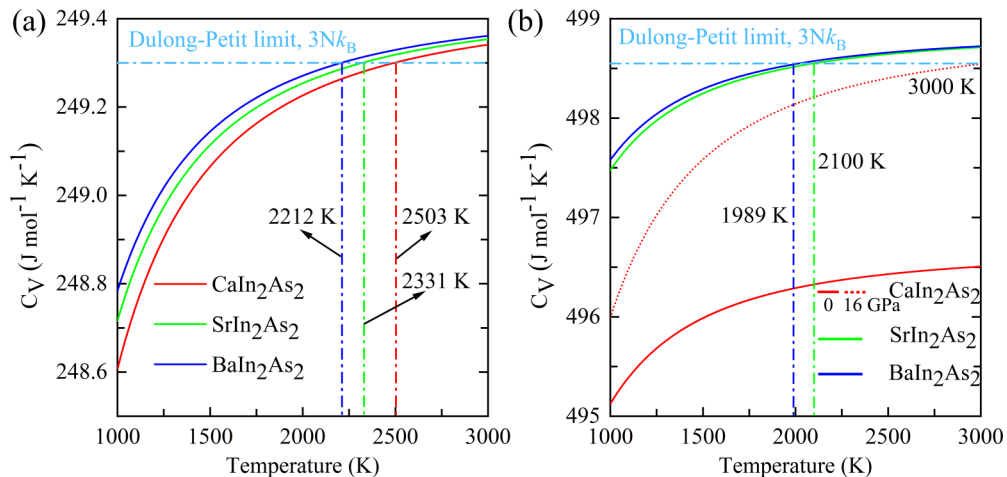


FIG. 8. (a) Hexagonal phase and (b) monoclinic phase $C_V - T$ curves. The cyan color dashed line indicates the Dulong-Petit limit.

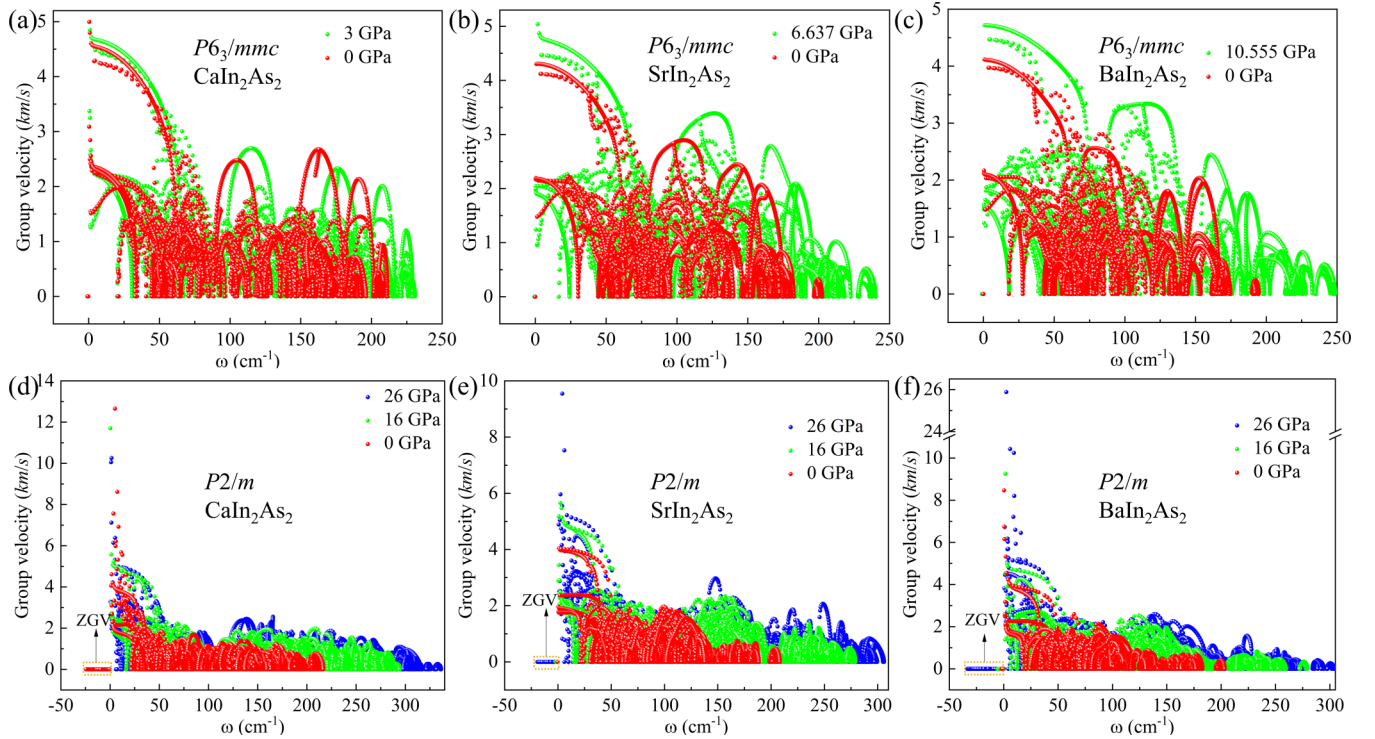


FIG. 9. Group velocity distributions dependent on phonon frequencies for the $P6_3/mmc$ phase (a) CaIn_2As_2 , (b) SrIn_2As_2 , (c) BaIn_2As_2 , and the $P2/m$ phase (d) CaIn_2As_2 , (e) SrIn_2As_2 , and (f) BaIn_2As_2 under different pressure.

relaxation time. The thermal conductivity can be initially predicted from v_g^2 . Figures S18 and S19 within the SM [30] give images of the frequency dependence of the squared group velocity v_{gi}^2 ($i = x, y, z$) in the three directions of the hexagonal and monoclinic phases AlIn_2As_2 under pressure. Closely related to the crystal structure, the $P6_3/mmc$ phase has similar group velocity evolution curves in the x and y directions. Therefore, for the $P6_3/mmc$ phase, we refer to the thermal conductivity transported within the octahedral inner layer as the in-plane thermal conductivity. Along the z direction, we refer to the out-of-plane thermal conductivity. The out-of-plane thermal conductivity of the hexagonal phase AlIn_2As_2 is slightly larger than the in-plane thermal conductivity. In the low-frequency region, thermal conduction is more favored along out-of-plane. However, the fluctuation phenomenon of the out-of-plane thermal conductivity is more pronounced, with zero thermal conductivity behavior in specific frequency regions, and thermal conductivity is frequency selective. Therefore, due to the octahedral lattice's hindrance, the out-of-plane thermal conduction behavior of the hexagonal phase AlIn_2As_2 is not as easy. For the monoclinic phase, as shown in Fig. S19 within the SM [30] AlIn_2As_2 has thermal conduction anisotropy in three directions, and the y direction is the main direction of thermal conduction (for CaIn_2As_2). This is because both the $P2/m$ phase structure along the x and z directions must traverse the A - As octahedral lattice [see the lattice structure in Fig. 1(c)]. In contrast, along the y direction, thermal conductivity is possible through the interstices of the octahedral lattice. For the monoclinic phase, the contribution of thermal conduction in the z direction is also significant to a certain extent. In summary, the x direction is the most difficult direction for thermal conduction in the monoclinic

phase, which is related to the smallest C_{11} elastic constant (see Fig. 11).

The pressures all enhance the group velocity for AlIn_2As_2 systems, leading to a shift of the group velocity towards high and low frequencies. The ZGV phenomenon resulting from shifting the monoclinic phase phonon spectrum towards lower frequencies under pressure directly reflects the softening of the phonon modes. The phonon frequency distribution of the monoclinic phase under pressure and the structure with atomic sites are given as shown in Fig. S20 within the SM [30]. We focus on the CaIn_2As_2 (0, 26 GPa), SrIn_2As_2 (26 GPa), and BaIn_2As_2 (26 GPa) systems that produce significant imaginary frequencies. The group velocity at the imaginary frequency (IFGV) of CaIn_2As_2 under pressure absence is mainly contributed by the $\text{In-}2n$ position (red dashed circle in Fig. S20(b) within the SM [30]) and the $\text{As-}2m$ position (blue dashed circle in Fig. S20(b) within the SM [30]). Most of the IFGV of CaIn_2As_2 under 26 GPa originates from not only the atomic contributions from the two Wyckoff sites mentioned above, but also the $\text{In-}2n$ site of the cyan color and the green-colored $\text{As-}2n$ site. For the IFGV of SrIn_2As_2 and BaIn_2As_2 at 26 GPa, there is also a contribution from the A atom in addition to the In and As atom contributions. The IFGV of SrIn_2As_2 under 26 GPa is mainly contributed by the Cyan-colored $\text{In-}2n$ site, the blue-colored $\text{As-}2m$ site and the A_2-1c site. BaIn_2As_2 , on the other hand, is primarily contributed by the black-colored $\text{In-}2m$ site, the green-colored $\text{As-}2n$ site, the A_1-1d site and the A_2-1c site. The main contributing atoms to the ZGV phenomenon produced by the softening of the phonon vibrational modes are also presented in Fig. S20(c) within the SM [30]. We can clearly find that the phonon mode softening is critically due to atomic vibrations across the zero

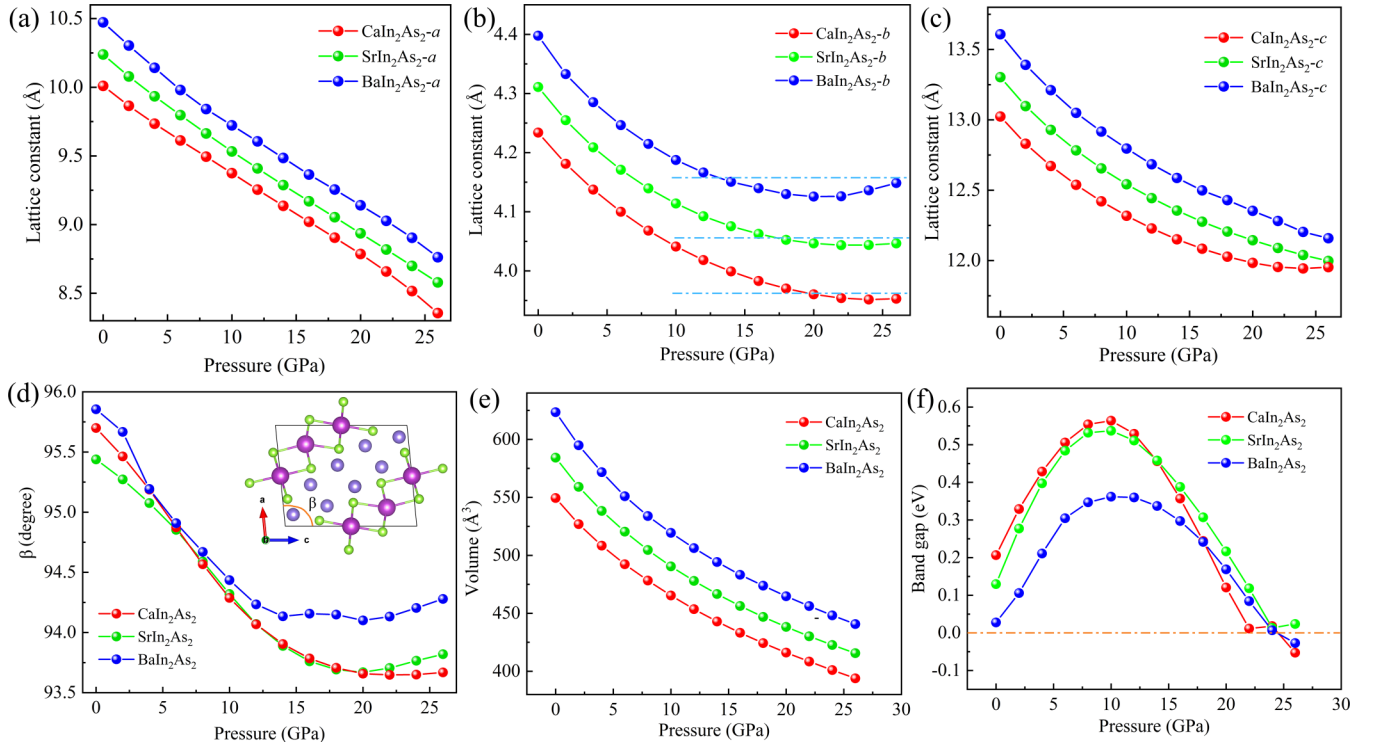


FIG. 10. Pressure-dependent evolution curves for AlIn_2As_2 of monoclinic phases ($P2/m$ space group). (a)–(c) Lattice constants, (d) ac -plane angle, (e) volume, and (f) band gap.

frequency near the In-In chain ([101] direction in Fig. S20 within the SM [30]). As seen in Table S1 within the SM [30], for the CaIn_2As_2 (0 GPa) system, the relatively large imaginary frequencies (below -0.08 cm^{-1}) are mainly contributed by IR-active A_u and Raman-active B_g . For AlIn_2As_2 under 26 GPa, on the other hand, the virtual frequencies are all mainly contributed by B_u . Therefore, softening the phonon modes at high pressure weakens the IR vibrational modes, A_u and B_u . It is interesting to note that the strange imaginary frequency of CaIn_2As_2 at 0 GPa also originates from the appearance of the Raman vibrational mode B_g , which should not have appeared in the acoustic branch. We can predict that along between the A -As octahedral layers (In-In atomic gaps)

is the direction of maximum probability of phonon softening and thermal conduction in the monoclinic phase AlIn_2As_2 .

IV. CONCLUSIONS

Based on DFT calculations, we have predicted the structural phase transition of AlIn_2As_2 materials under pressure and characterized their mechanical and thermal properties. Firstly, enthalpy of formation and phonon spectroscopy calculations confirm the structural phase transition of AlIn_2As_2 under pressure. Moreover, the low-pressure phase of $\text{Ca}(\text{Sr})\text{In}_2\text{As}_2$ materials is hexagonal, while the high-pressure phase is monoclinic. But BaIn_2As_2 always prefers to form monoclinic phases. Next, we deeply analyze the symmetries of different

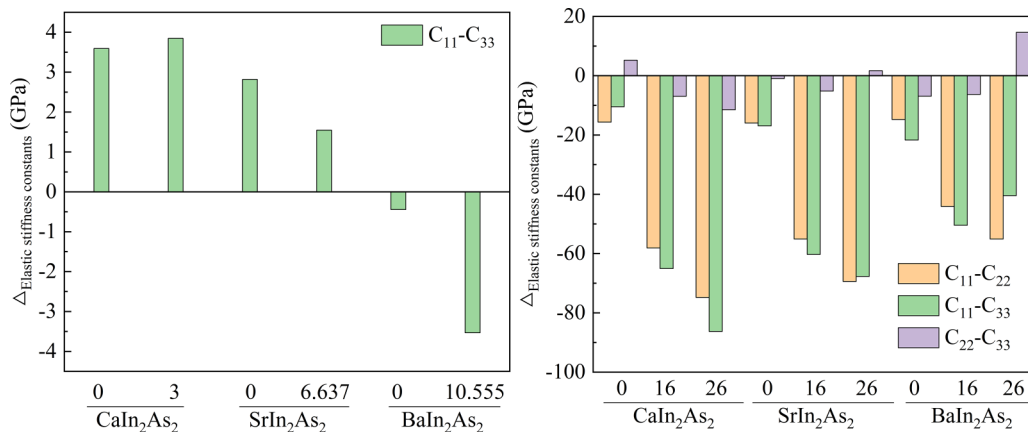


FIG. 11. The difference in elastic stiffness constants for the AlIn_2As_2 system belonging to the (a) $P6_3/mmc$ (b) $P2/m$ space group corresponds to the data in Table VII.

TABLE VII. Elastic stiffness constants C_{ij} (GPa), bulk modulus B (GPa), shear modulus G (GPa), Young's modulus E (GPa), and Poisson's ratio ν from different space group: monoclinic phases ($P2/m$) and hexagons ($P6_3/mmc$) for AlIn_2As_2 under different pressures.

Phase	Material	Pressure (GPa)	C_{11}	C_{12}	C_{13}	C_{22}	C_{23}	C_{33}	C_{44}	C_{15}	C_{25}	C_{35}	C_{55}	C_{64}	C_{66}	B	G	E	ν	
$P2/m$	CaIn_2As_2	0	74.652	32.609	23.923	90.334	16.44	85.140	20.326	1.384	1.644	1.356	23.806	2.523	35.872	43.856	27.09	67.386	0.244	
		16	87.617	69.327	56.958	145.725	49.167	152.6681	32.712	-1.610	2.573	8.960	33.992	8.477	45.378	79.655	33.877	88.987	0.314	
		26	87.971	88.590	92.947	162.791	90.496	174.268	47.198	-5.017	-1.149	6.888	42.145	5.176	52.504	97.323	32.028	86.503	0.353	
	SrIn_2As_2	0	70.374	32.771	20.298	86.344	12.462	87.300	19.110	1.273	2.209	2.041	22.938	3.166	38.071	41.525	26.743	66.033	0.235	
		16	89.850	75.557	49.900	144.961	48.398	150.152	32.796	-1.868	2.524	8.731	31.823	6.686	49.650	79.198	33.985	89.161	0.313	
		26	99.850	101.189	75.526	169.273	88.088	167.593	47.132	-4.574	1.583	7.289	37.002	4.308	52.987	100.894	34.213	92.168	0.348	
$P6_3/mmc$	BaIn_2As_2	0	64.772	32.308	17.798	79.566	10.205	86.469	17.118	1.027	2.697	2.239	20.904	3.411	38.577	38.900	25.110	61.958	0.235	
		16	93.718	81.344	47.987	137.817	51.239	144.157	29.619	-3.343	2.288	6.966	27.790	4.168	49.850	80.026	31.199	82.778	0.328	
		26	106.797	109.860	68.359	161.884	95.283	147.284	41.861	-4.215	3.589	2.877	29.211	0.906	50.607	99.001	28.757	78.603	0.369	
	CaIn_2As_2	0	88.379	24.956	25.243			84.788	25.879							31.712	45.779	29.093	72.022	0.238
		3	101.826	32.380	34.540			97.980	26.634							34.723	56.027	30.820	78.133	0.268
		0	82.964	23.707	24.423			80.149	26.357							29.629	43.437	28.072	69.289	0.234
BaIn_2As_2	6.637	107.796	39.817	45.241			106.251	25.065							33.989	64.672	29.423	76.645	0.302	
	10.555	112.472	54.953	55.710			75.69	25.760							25.973	41.077	25.626	63.643	0.242	

space groups, propose the structural phase transition path of $P6_3/mmc \rightarrow R\bar{3}m \rightarrow C2/m \rightarrow P2/m$ with $C2/m$ as the intermediate phase, and establish the physical correlation behind the structural phase transition.

We then also obtain a variety of elastic moduli based on the elastic stiffness matrix and further analyze the crystal anisotropy, chemical bonding properties, hardness, toughness, and other mechanical properties of the $P6_3/mmc$ phase and the $P2/m$ phase AlIn_2As_2 . Among them, we have deeply investigated the crystal anisotropy transition of AlIn_2As_2 series materials based on pressure. Pressure will induce a transition from isotropy to anisotropy in the AlIn_2As_2 of the hexagonal phase. Pressure will also enhance the crystal anisotropy in the monoclinic phase. In addition, the bulk anisotropy of these mechanical parameters (G, E, LC, ν) depends differently on the plane anisotropy of the $xy, yz,$ and xz planes. We also find that pressure will induce a transition from brittle to ductile in the AlIn_2As_2 of the monoclinic and hexagonal phases. And it is found that AlIn_2As_2 can be transformed into NPR materials under both compressive and tensile stresses. At the same time, we predict the hardness of different structural phases of AlIn_2As_2 that depend on the band gap.

On the other hand, we postulate that downward pressure can effectively raise materials' structural phase transition temperature and report their thermal properties such as heat capacity, entropy and free energy. Pressure is favored to enhance the heat capacity profile of the softened monoclinic CaIn_2As_2 to reach the Dulong-Petit limit. Thus, we determined that $\text{Ca}(\text{Sr})\text{In}_2\text{As}_2$ is hexagonal at low pressure. BaIn_2As_2 enjoys a monoclinic phase but will be in the NPMP phase with similar energies of the monoclinic and hexagonal phases if stretched. At low temperatures, AlIn_2As_2 materials prefer to form the hexagonal phase, but they will transform into a monoclinic phase under high temperatures. Moreover, the pressure is favorable to increase the transition temperature of the structural phase. A theoretical basis is laid for a better study of the thermoelectric properties of AlIn_2As_2 . In a nutshell, our study confirms the mechanical properties and thermal behavior behind the structural phase transition of this family of materials.

ACKNOWLEDGMENTS

We acknowledge the financial support by the National Natural Science Foundation of China (Grant No. 11874113) and the Natural Science Foundation of Fujian Province of China (Grant No. 2020J02018). The work was carried out at National Supercomputer Center in Tianjin, and the calculations were performed on TianHe-1(A).

APPENDIX A: COMPUTATIONAL DETAILS

1. Phonon and thermodynamic properties calculation

For the phonon calculation, the density functional perturbation theory (DFPT) in PHONOPY [40] was applied to combine with VASP in the structures of the $P6_3/mmc, R\bar{3}m,$ and $P2/m$ space groups by the $2 \times 2 \times 1, 2 \times 2 \times 2,$ and $1 \times 2 \times 1$ supercells, respectively.

TABLE VIII. The reciprocal of Pugh's ratio B/G , Kleinman's parameter ξ , Cauchy's pressure P_C (GPa), chemical bond type, universal anisotropy index (A_u), and Log-Euclidean anisotropy (A_L) from different space group: monoclinic phases ($P2/m$) and hexagons ($P6_3/mmc$) for AlIn_2As_2 under different pressures.

Phase	Material	Pressure (GPa)	B/G	ξ	P_C^a (Chemical bond)	P_C^c (Chemical bond)	A_u	A_L
$P2/m$	CaIn_2As_2	0	1.619 (brittle)	0.73	12.3 (MLB)		0.315	0.134
		16	2.351 (ductile)	1.35	36.6 (MLB)		0.910	0.357
		26	3.04 (ductile)	1.81	41.4 (MLB)		2.883	0.973
	SrIn_2As_2	0	1.553 (brittle)	0.78	13.7 (MLB)		0.491	0.207
		16	2.330 (ductile)	1.45	42.8 (MLB)		1.022	0.398
		26	2.949 (ductile)	1.83	54.1 (MLB)		1.753	0.639
	BaIn_2As_2	0	1.549 (brittle)	0.83	15.2 (MLB)		0.701	0.291
		16	2.565 (ductile)	1.51	51.7 (MLB)		1.204	0.468
		26	3.443 (ductile)	1.87	68.0 (MLB)		2.255	0.794
$P6_3/mmc$	CaIn_2As_2	0	1.574 (brittle)	0.50	-0.6 (CLB)	-6.8 (CLB)	0.044	0.020
		3	1.818 (ductile)	0.56	7.9 (MLB)	-2.3 (CLB)	0.072	0.032
	SrIn_2As_2	0	1.547 (brittle)	0.51	-1.9 (CLB)	-5.9 (CLB)	0.014	0.006
		6.637	2.198 (ductile)	0.63	20.2 (MLB)	5.8 (MLB)	0.094	0.041
	BaIn_2As_2	0	1.603 (brittle)	0.55	-1.7 (CLB)	-2.7 (CLB)	0.000	0.000
		10.555	3.104 (ductile)	0.81	37.7 (MLB)	26.2 (MLB)	0.275	0.120

Thermodynamic properties, including heat capacity, internal energy, entropy, and Helmholtz free energy, were calculated by the following equations [41,42]:

$$C_v = \frac{k_B}{N_q} \sum_{q,j} \left(\frac{\hbar\omega_{qj}}{2k_B T} \right)^2 \text{cosech}^2 \left(\frac{\hbar\omega_{qj}}{2k_B T} \right), \quad (\text{A1})$$

$$U_{\text{vib}}(T) = \frac{1}{N_q} \sum_{q,j} \hbar\omega_{qj} \left[\frac{1}{e^{\hbar\omega_{qj}/k_B T} - 1} + \frac{1}{2} \right], \quad (\text{A2})$$

$$S_{\text{vib}}(T) = \frac{k_B}{N_q} \sum_{q,j} \left[\frac{\hbar\omega_{qj}}{k_B T (e^{\hbar\omega_{qj}/k_B T} - 1)} - \ln \left(1 - e^{-\frac{\hbar\omega_{qj}}{k_B T}} \right) \right], \quad (\text{A3})$$

$$F(T) = \frac{1}{N_q} \sum_{q,j} \left[\frac{\hbar\omega_{qj}}{2} + k_B T \ln(1 - e^{-\hbar\omega_{qj}/k_B T}) \right], \quad (\text{A4})$$

$$\Delta F_{P2/m-P6_3/mmc}(T) = \Delta E + \Delta U_{\text{vib}}(T) - T \Delta S(T), \quad (\text{A5})$$

where k_B is the Boltzmann constant, N_q is the number of wave vectors q , and ω_{qj} is the vibrational frequency of the phonon mode qj . Δ in Eq. (A5) denotes each physical parameter difference, where ΔE is the total energy difference calculated by VASP.

2. Mechanical properties characterization

a. Elastic moduli and mechanical stability criteria

The elastic modulus formulas for the hexagonal and monoclinic phases are from Ref. [43] and Ref. [44], respectively. The mechanical stability criterion is from Ref. [45]. The Voigt Reuss-Hill [46] approximation is the arithmetic mean of the Voigt [47] and Reuss bounds [48]. B denotes the bulk modulus, G denotes the shear modulus, E denotes Young's modulus, and ν denotes Poisson's ratio. According to the Voigt-Reuss-Hill approximation [46], $X_H = (1/2)(X_R + X_V)$, $X = B, G$. Furthermore, Young's modulus E and Poisson's ratio ν are

derived from Eq. (A6),

$$E = \frac{9BG}{3B + G}, \quad \nu = \frac{3B - 2G}{6B + 2G}. \quad (\text{A6})$$

The independent elastic stiffness constants C_{ij} of hexagonal phase include C_{11} , C_{33} , C_{44} , C_{12} , and C_{13} . The modulus can be described as follows:

$$B_V = \frac{1}{9}[2(C_{11} + C_{12}) + 4C_{13} + C_{33}], \quad (\text{A7})$$

$$G_V = \frac{1}{30}(M + 12C_{44} + 12C_{66}), \quad (\text{A8})$$

$$B_R = \frac{C^2}{M}, \quad (\text{A9})$$

$$G_R = \frac{\frac{5}{2}(C^2 C_{44} C_{66})}{3B_V C_{44} C_{66} + C^2(C_{44} + C_{66})}, \quad (\text{A10})$$

where

$$M = C_{11} + C_{12} + 2C_{33} - 4C_{13},$$

$$C^2 = (C_{11} + C_{12})C_{33} - 2C_{13}^2.$$

The mechanical stability criteria are given via

$$C_{44} > 0, \quad C_{11} > |C_{12}|, \quad (C_{11} + 2C_{12})C_{33} > 2C_{13}^2.$$

As for monoclinic phase, the independent C_{ij} can be indicated to C_{11} , C_{22} , C_{33} , C_{44} , C_{55} , C_{66} , C_{12} , C_{13} , C_{23} , C_{15} , C_{25} , C_{35} , and C_{64} . The modulus can be described as follows:

$$B_V = \frac{1}{9}[C_{11} + C_{22} + C_{33} + 2(C_{12} + C_{13} + C_{23})], \quad (\text{A11})$$

$$G_V = \frac{1}{15}[C_{11} + C_{22} + C_{33} + 3(C_{44} + C_{55} + C_{66}) - (C_{12} + C_{13} + C_{23})]. \quad (\text{A12})$$

$$B_R = \Omega[a(C_{11} + C_{22} - 2C_{12}) + b(2C_{12} - 2C_{11} - C_{23}) + c(C_{15} - 2C_{25}) + d(2C_{12} + 2C_{23} - C_{13} - 2C_{22}) + 2e(C_{25} - C_{15}) + f]^{-1}, \quad (\text{A13})$$

$$G_R = 15 \left\{ \begin{aligned} &4a(C_{11} + C_{22} + C_{12}) + b(C_{11} - C_{12} - C_{23}) \\ &+ c(C_{15} + C_{25}) + d(C_{22} - C_{12} - C_{23} - C_{13}) \\ &+ e(C_{15} - C_{25}) + f \end{aligned} \right\} / \Omega + 3 \left[\frac{g}{\Omega} + \frac{C_{44} + C_{66}}{C_{44}C_{66} - C_{64}^2} \right]^{-1}, \quad (\text{A14})$$

$$\begin{aligned} a &= C_{33}C_{55} - C_{35}^2, & b &= C_{23}C_{55} - C_{25}C_{35}, \\ c &= C_{13}C_{35} - C_{15}C_{33}, & d &= C_{13}C_{55} - C_{15}C_{35}, \\ e &= C_{13}C_{25} - C_{15}C_{23}, \\ f &= C_{11}(C_{22}C_{55} - C_{25}^2) - C_{12}(C_{12}C_{55} - C_{15}C_{25}) \\ &\quad + C_{15}(C_{12}C_{25} - C_{15}C_{22}) + C_{25}(C_{23}C_{35} - C_{25}C_{33}), \\ g &= C_{11}C_{22}C_{33} - C_{11}C_{23}^2 - C_{22}C_{13}^2 - C_{33}C_{12}^2 + 2C_{12}C_{13}C_{23}, \\ \Omega &= 2[C_{15}C_{25}(C_{33}C_{12} - C_{13}C_{23}) + C_{15}C_{35}(C_{22}C_{13} - C_{12}C_{23}) \\ &\quad + C_{25}C_{35}(C_{11}C_{23} - C_{12}C_{13})] - [C_{15}^2(C_{22}C_{33} - C_{23}^2) \\ &\quad + C_{25}^2(C_{11}C_{33} - C_{13}^2) + C_{35}^2(C_{11}C_{22} - C_{12}^2)] + gC_{55}. \end{aligned}$$

The criteria for mechanical stability are given via

$$\begin{aligned} C_{11} > 0, \quad C_{22} > 0, \quad C_{33} > 0, \quad C_{44} > 0, \quad C_{55} > 0, \quad C_{66} > 0, \\ [C_{11} + C_{22} + C_{33} + 2(C_{12} + C_{13} + C_{23})] > 0, \\ (C_{33}C_{55} - C_{35}^2) > 0, \quad (C_{44}C_{66} - C_{46}^2) > 0, \\ (C_{22} + C_{33} - 2C_{23}) > 0, \\ [C_{22}(C_{33}C_{55} - C_{35}^2) + 2C_{23}C_{25}C_{35} - C_{23}^2C_{55} \\ - C_{25}^2C_{33}] > 0, \\ \{2[C_{15}C_{25}(C_{33}C_{12} - C_{13}C_{23}) + C_{15}C_{35}(C_{22}C_{13} \\ - C_{12}C_{23}) \\ + C_{25}C_{35}(C_{11}C_{23} - C_{12}C_{13})] - [C_{15}^2(C_{22}C_{33} - C_{23}^2) \\ + C_{25}^2(C_{11}C_{33} - C_{13}^2) + C_{35}^2(C_{11}C_{22} - C_{12}^2)] \\ + gC_{55}\} > 0. \end{aligned}$$

b. Crystal anisotropy calculation

Since Zener anisotropy [49] and Chung-Buessem anisotropy [50] indices are only applicable to cubic crystals, we used the universal anisotropy index A_U [51] and log-Euclidean anisotropy index A_L [52] for the anisotropy analysis of $P6_3/mmc$ and $P2/m$ phases. A_U takes into account all the stiffness coefficients to define the anisotropy, exploiting the tensor nature of the elastic stiffness. The specific expression is shown in Eq. (A15). The expression for A_L with respect to the modulus of elasticity is given by Eq. (A16),

$$A_U = 5 \frac{G_V}{G_R} + \frac{B_V}{B_R} - 6, \quad (\text{A15})$$

$$A_L = \sqrt{\left[\ln \left(\frac{B_V}{B_R} \right) \right]^2 + 5 \left[\ln \left(\frac{G_V}{G_R} \right) \right]^2}. \quad (\text{A16})$$

The value of the anisotropy parameter (A_U and A_L) is ≥ 0 . They characterize the strength of the crystal anisotropy, and their convergence to zero implies crystal isotropy.

c. Bonding information calculation

The Kleinman parameter (ξ) allows evaluation of the stability of the solid under stretching or bending [53], which is defined as

$$\xi = \frac{C_{11} + 8C_{12}}{7C_{11} - 2C_{12}}.$$

$\xi = 0$ and 1 imply that bond bending and stretching will be dominated, respectively.

The Cauchy pressure (P_C) can also be used to describe the brittleness and ductility of a metal or compound. For hexagonal crystal systems, it is defined as $P_C^a = C_{13} - C_{44}$ and $P_C^b = C_{12} - C_{66}$ [54].

d. Hardness prediction

First-principles calculations provide a good assessment of the various mechanical properties of a solid. However, DFT does not give a reasonable evaluation of hardness directly. We predict hardness based on the following semi-empirical relationships to describe the mechanical behavior of AlIn_2As_2 fully [55–59],

$$H_{1a} = 0.1475G, \quad H_{1b} = 0.0607E \quad [55],$$

$$H_2 = 0.1769G - 2.899 \quad [56],$$

$$H_3 = 0.0635E \quad [57],$$

$$H_4 = \frac{(1 - 2\nu)B}{6(1 + \nu)} \quad [58],$$

$$H_5 = 2 \left(\frac{G^3}{B^2} \right)^{0.585} - 3 \quad [59]. \quad (\text{A17})$$

In addition, Ivanovskii is well placed to summarize these semi-experiences [60]. Furthermore, Sobhit Singh calculated the hardness of various materials and compared it with experimental data to choose the semi-empirical calculation of the most appropriate hardness based on the material's space group and band gap [61] (see Table II).

ELATools [62], MechElastic [61,63], and ELATE [64] programs were used for the calculation of mechanical parameters and visualization of the modulus.

APPENDIX B: ADDITIONAL RESULTS

1. Evolution of lattice parameters under pressure

The application of pressure will first directly change the lattice parameters of the material. The $R\bar{3}m$ and $P6_3/mmc$ space groups, which also belong to the hexagonal crystal system, have similar pressure-dependent lattice parameter evolution patterns. As the reported earlier, the lattice constants of AlIn_2As_2 materials with the $P6_3/mmc$ space group both decrease with increasing pressure. In addition, the bond angles of the hexagonal crystal system are robust to pressure, always maintaining $\alpha = 90^\circ$, $\beta = 90^\circ$, $\gamma = 120^\circ$. However, the bond angle β of monoclinic crystal systems is very sensitive to pressure. As shown in Fig. 10(d), the bond angles of the three

systems first decrease then increase with increasing pressure, especially for the SrIn_2As_2 and BaIn_2As_2 systems, where this evolution regular is more obvious. The lattice constants a , b , and c all show a general trend of becoming smaller with the applied positive pressure [see Fig. 10(a)–10(c)]. The lattice constant a is almost linear with pressure, and the lattice constants b and c are gradually decreasing curves. It is important to note that the lattice constant b of BaIn_2As_2 becomes larger again under high pressure. As shown in Fig. 10(e), the volume-pressure curve fully reflects the effect of pressure. As with the lattice parameters, the volume shows a positive correlation with the radius of the A atom (BaIn_2As_2 is the largest and CaIn_2As_2 the smallest). As shown in Fig. 10(f), the band gaps of all three AlIn_2As_2 systems show a trend of increasing and then decreasing under pressure, and all have a band gap maximum around 10 GPa. Narrow band gaps are often accompanied by the nontrivial topological properties of band inversion.

2. Symmetry transformation of point group

For the space group $R\bar{3}m$ with point group $D_{3d}(-3m)$,

$$\Gamma_{\text{acoustic}} = A_{2u} + E_u,$$

$$\Gamma_{\text{optic}} = 2A_{1g} + 2A_{2u} + 2E_g + 2E_u.$$

In total, there are 15 vibrational modes, five nondegenerate A_{1g} and A_{2u} modes, and five doubly degenerate E_g and E_u modes. Among them, optical vibrations $2A_{1g} + 2E_g$ are Raman (R) active, while optical modes $2A_{2u} + 2E_u$ are infrared Raman (IR) active,

$$R(A_{1g}) = \begin{pmatrix} a & d & 0 \\ d & a & 0 \\ 0 & 0 & b \end{pmatrix}, \quad R(E_{g,1}) = \begin{pmatrix} c & 0 & 0 \\ 0 & -c & d \\ 0 & d & 0 \end{pmatrix},$$

$$\text{and } R(E_{g,2}) = \begin{pmatrix} 0 & -c & -d \\ -c & 0 & 0 \\ -d & 0 & 0 \end{pmatrix}.$$

For the space group $P2/m$ with point group $C_{2h}(2/m)$,

$$\Gamma_{\text{acoustic}} = A_u + 2B_u,$$

$$\Gamma_{\text{optic}} = 18A_g + 10A_u + 9B_g + 20B_u.$$

In total, there are 60 vibrational modes, all of them are nondegenerate A_g , B_g , A_u , and B_u modes. Here, the optical vibration $10A_u + 20B_u$ is infrared (IR) active, while the optical mode $18A_g + 9B_g$ is Raman (R) active. The corresponding mode activity and symmetry at the Γ point are shown in Table IV,

$$R(A_g) = \begin{pmatrix} a & d & 0 \\ d & b & 0 \\ 0 & 0 & c \end{pmatrix}; \quad R(B_g) = \begin{pmatrix} 0 & 0 & e \\ 0 & 0 & f \\ e & f & 0 \end{pmatrix},$$

$$T = \begin{pmatrix} -\frac{2}{3} & -1 & -\frac{4}{3} & -\frac{1}{3} \\ \frac{2}{3} & -1 & \frac{4}{3} & \frac{1}{3} \\ -\frac{1}{3} & 0 & \frac{1}{3} & -\frac{1}{6} \end{pmatrix}, \quad (\text{B1})$$

$$GS = \begin{pmatrix} 0 & -1 & \frac{2}{3} & 0 \\ 0 & -1 & -\frac{2}{3} & 0 \\ 1 & 0 & -\frac{2}{3} & 0 \end{pmatrix}; \quad EAN = \begin{pmatrix} -1 & 0 & -1 \\ 0 & 1 & 0 \\ -1 & 0 & -2 \\ 0 & 0 & 0 \end{pmatrix};$$

$$LC = \begin{pmatrix} -\frac{2}{3} & -1 & -\frac{4}{3} \\ \frac{2}{3} & -1 & \frac{4}{3} \\ -\frac{1}{3} & 0 & -\frac{1}{3} \end{pmatrix}; \quad EEN = \begin{pmatrix} 1 & 0 & 0 & \frac{1}{2} \\ 0 & 1 & 0 & 0 \\ 0 & 0 & 1 & 0 \end{pmatrix}.$$

The structural transformation is performed in Bilbao Crystallographic Server [65]. The chain of transformation relations from the $R\bar{3}m$ to the $P2/m$ structure includes three transformation matrices channels (P_i, p) ($i = 1 - 6$) [see Eq. (B2)]. These matrices achieve the symmetric operational transformation from the hexagonal to the monoclinic phase,

$$(P_1|p) = \begin{pmatrix} 0 & 1 & 2/3 & |0 \\ 0 & 0 & 4/3 & |0 \\ 1 & 0 & -2/3 & |0 \end{pmatrix};$$

$$(P_2|p) = \begin{pmatrix} -2/3 & 1 & 0 & | -1/6 \\ -4/3 & 0 & 0 & | -1/3 \\ -4/3 & 0 & 1 & | -1/3 \end{pmatrix};$$

$$(P_3|p) = \begin{pmatrix} 0 & 0 & -4/3 & | -1/3 \\ 0 & 1 & -2/3 & | -1/6 \\ 1 & 0 & -2/3 & | -1/6 \end{pmatrix};$$

$$(P_4|p) = \begin{pmatrix} -4/3 & 0 & 4/3 & |0 \\ -2/3 & 1 & 2/3 & |0 \\ 1/3 & 0 & -4/3 & |0 \end{pmatrix};$$

$$(P_5|p) = \begin{pmatrix} -2/3 & -1 & 0 & |0 \\ 2/3 & -1 & 0 & |0 \\ -4/3 & 0 & 1 & |0 \end{pmatrix};$$

$$(P_6|p) = \begin{pmatrix} 2/3 & -1 & -2/3 & | -1/6 \\ -2/3 & -1 & 2/3 & | 1/6 \\ 1/3 & 0 & -4/3 & | -1/3 \end{pmatrix}. \quad (\text{B2})$$

3. Mechanical properties characterization

a. Calculation of elastic constants

Stress and strain tend to change the elastic tensor information of the solid materials, so it is crucial to study the mechanical properties of materials under pressure, such as Young's modulus, shear modulus, p -wave modulus, Poisson's ratio, anisotropy index, Kleinman's parameter, Cauchy pressure, Pugh's ratio, and hardness information. Our calculated results under all pressures satisfy the criteria for mechanical stability in Appendix A 2 a, representing that all AlIn_2As_2 systems are mechanically stable. We calculated the elastic constants for the two phases at different pressures as shown in Table VII. C_{11} , C_{22} , and C_{33} denote the linear compression resistance along the a , b , and c axes, respectively. For hexagonal phase, $C_{11} = C_{22} \neq C_{33}$ and C_{33} are smaller than C_{11} for all systems except BaIn_2As_2 , indicating that the c axis is more compressible than the a axis and b axis, which also reflects the weaker chemical bonding in the c axis than the a axis and b axis. In contrast, C_{33} is larger than C_{11} in BaIn_2As_2 of the hexagonal phase resulting in the c axis being more incompressible than the $a(b)$ axis, indicating that the c -

directional chemical bonding of BaIn_2As_2 is more stable than the $a(b)$ directional. This easily compressible direction evaluates the maximum probability direction of the structure phase transition. Due to the weaker bonding in the ab plane, the octahedral layers in Fig. 1(a) are more easily deformed within the layers than between them. This anomalous behavior of the hexagonal phase BaIn_2As_2 compared to CaIn_2As_2 , SrIn_2As_2 perfectly explains the previous experimental result for their different structural phases. As can be seen from Fig. 11(a), the bonding strengths differences between the $a(b)$ axis and c axis of CaIn_2As_2 and SrIn_2As_2 are positive, while the bonding in the in-plane (C_{11} and C_{22}) of BaIn_2As_2 is weaker than that in the out-plane (C_{33}) (about -3.5 GPa). This result implies that CaIn_2As_2 and SrIn_2As_2 are prone to structural phase transitions in the c -direction, while BaIn_2As_2 is prone to structural phase transitions in the in-plane. For the monoclinic phase [see Table VII and Fig. 11(a)], satisfying $C_{11} \neq C_{22} \neq C_{33}$, C_{11} is smaller than C_{22} and C_{33} for all systems, and the difference $\Delta_{C_{11}-C_{ij}}$ ($i = j = 2, 3$) becomes more significant as the pressure is applied except for BaIn_2As_2 which becomes smaller under 26 GPa. Without pressure, C_{22} of CaIn_2As_2 is maximum while C_{33} of SrIn_2As_2 and BaIn_2As_2 is maximum. With applying pressure, C_{22} and C_{33} compete, CaIn_2As_2 becomes maximum at 16 GPa for C_{33} while SrIn_2As_2 and BaIn_2As_2 reverse to the maximum at 26 GPa for C_{22} . In conclusion, the monoclinic phase of AlIn_2As_2 , especially after applying pressure, has weak bonding in the a axis, and it is relatively easy to peel in that direction.

b. Elastic modulus analysis

The bulk modulus B is a physical measure of the material's ability to resist compression: the more significant the B , the more excellent the resistance to compression and the smaller the compressibility. The B of Hill approximation is related to B_V and B_R , and the B of both two phases can be explicitly calculated by Eqs. (A7), (A9), (A11), and (A13). As shown in Table VII, the B of the monoclinic phase is generally smaller and more compressible than the hexagonal phase, which is related to the low-symmetry structure of the monoclinic. The bulk modulus of the hexagonal phase obtained from the elastic constants remarkably agrees with the fit of the B-M equation reported in our previous paper [20]. The bulk moduli of the present paper (Ref. [20]) are 45.779 GPa (46.3 GPa), 43.437 GPa (43.8 GPa), and 41.077 GPa (41.7 GPa) for the hexagonal phases CaIn_2As_2 , SrIn_2As_2 , and BaIn_2As_2 , respectively. Our results also show that pressure can effectively enhance the resistance to compression of both two phases, which can be explained by the decrease in lattice parameters after compression [see Figs. 3(a)–3(e) and Fig. S2 in Ref. [20]].

The shear modulus G reflects the ratio of stress to strain under shear deformation. The larger the G , the greater the resistance to shear deformation. G can also be calculated from Eqs. (A8), (A10), (A12), and (A14). The relationship between the two structural phases of G and the trend of change under pressure is similar to that of B . The applied pressure can enhance the shear deformation resistance of most of the systems. However, it reduced again that the shear deformation resistance of CaIn_2As_2 at 26 GPa and BaIn_2As_2 (both two

phases) under higher pressures. Without pressure, B and G of both space groups decrease as the atomic number of A increases.

Young's modulus E is an important index to characterize the stiffness of solid materials reflecting the system's resistance to elastic deformation. Poisson's ratio ν reflects the stability of the solid against shear deformation. They can be calculated from B and G by Eq. (A6). Also given by Table VII, the variation regular of E under pressure is consistent with G and B for the $P2/m$ phase and $P6_3/mmc$ phase, respectively. Poisson's ratio ν is stable at $-1 \sim 0.5$ under linear elastic shear deformation. Based on the data in Table VII, we can quickly determine that ν is positive and within the stability range, again proving that all systems are mechanically stable.

c. Pressure affects crystal anisotropy results

In order to visualize the effect of pressure on each elastic modulus, we calculated their 2D projections in a specific plane (see Figs. S6–S10 within the SM [30]). The hexagonal phase (see Figs. S6 and S7 within the SM [30]) tends to be more isotropic than the monoclinic phase due to the higher symmetry and the neater octahedral lattice, especially with the most significant isotropy for each BaIn_2As_2 mechanics without pressure (compare with Figs. S6 and S10 within the SM [30]). When the pressure modulates AlIn_2As_2 as a zero-bandgap solid material, the linear compression maintains isotropy. Since the pressure values of induced zero bandgaps for CaIn_2As_2 and SrIn_2As_2 are weak, the variation of each mechanical quantity is not significantly different from that under no pressure. However, we can see that a pressure of 10.555 GPa will induce the change of G , E , ν of BaIn_2As_2 from isotropic to anisotropic. For CaIn_2As_2 in the monoclinic phase (see Fig. S8 within the SM [30]), the following conclusions can be drawn as the pressure increases: (1) The anisotropy of the G -minimum positive (green curve) and E -maximum positive increase, especially in the $xy(001)$ and $xz(010)$ planes. This phenomenon is because the difference between C_{22} (C_{33}) and C_{11} increases sharply under pressure. (2) The maximum positive value of linear compression changes from almost isotropic to polarized in the x direction (a axis). The maximum positive value in the yz plane disappears due to the pressure effect. In contrast, the minimum negative value polarization along the z direction (c axis) appears under 26 GPa pressure (red curve). (3) At 26 GPa, the minimum NPR phenomenon occurs (red curve in Fig. S8 within the SM [30]). For SrIn_2As_2 and BaIn_2As_2 in the monoclinic phase of Figs. S9 and S10 within the SM [30], the more obvious difference is that the pressure-induced linear compression at 26 GPa has a minimum negative value along the y direction (b axis), but not z direction. Second, the maximum value of linear compression and the minimum positive value of ν (green curve) are observed in the yz plane under 26 GPa, which are not visible in CaIn_2As_2 . Also, the anisotropy of the maximum positive value of ν (blue curve) for the CaIn_2As_2 and SrIn_2As_2 regimes at 26 GPa is weaker than that of BaIn_2As_2 in yz plane.

Furthermore, we calculate the 3D space-dependent mechanical quantities (G , E , B , and ν) for the two phases as BaIn_2As_2 (see Figs. S1–S5 within the SM [30]). It can be

visualized that the AlIn_2As_2 of the intrinsic hexagonal phase is indeed highly isotropic, while the monoclinic phase exhibits anisotropy.

d. Chemical bonding, brittleness, and hardness prediction

The Pugh's ratio (G/B) or B/G ratio defines the ductility or brittleness of a solid. With $B/G = 1.75$ as the threshold value, a material with $B/G > 1.75$ is considered ductile, while the opposite is considered brittle. From Table VIII, we can find that the AlIn_2As_2 system without pressure behaves as brittle, while B/G increases and transforms into ductile after applying pressure. The ξ parameter evaluates whether the material is bending dominated or stretch dominated. When the value is close to 0, the system is bending-dominated, and close to 1, it is tensile dominated. As seen in Table VIII, the monoclinic phase has a larger ξ than the hexagonal phase, and the larger the A atomic number, the larger the ξ . Moreover, all the AlIn_2As_2 systems we consider, whether pressurized or not, exhibit stretching dominance. As demonstrated in Table VIII, Cauchy's pressure P_C can effectively assess the type of chemical bonding. The monoclinic phase AlIn_2As_2 tends to bond in a metallic manner MLB, and the strength of this bonding is proportional to the ionization energy of the A ion. Moreover, the pressure favors the enhancement of the metallic character of the system. The hexagonal phase of AlIn_2As_2 has both Cauchy's pressures (P_C^a and P_C^c) negative in the absence of pressure, indicating a tendency to form covalent bonds CLB. In addition, the pressure will reverse the sign of Cauchy's pressure, and the bonding style changes to a metallic bonding-dominated situation.

Hardness can adequately describe the mechanical behavior of solids and is one of the critical factors in practical production processes. We evaluate the hardness of AlIn_2As_2 in different states according to the six semi-empirical formulas of Eq. (A17) and the judgment guide of Table II. The Vickers hardness is calculated from H_{1b} or H_3 for the hexagonal phase of AlIn_2As_2 with $P6_3/mmc$ space group, semiconductors at 0 GPa ($0 < E_g < 2$ eV). As shown in the orange and red curves in Fig. 12, they are higher than other calculations. When applying a pressure that induces a zero bandgap ($E_g = 0$), the crystal hardness tends to be expressed by H_4 , with a reduced hardness (green curve). For the monoclinic phase of the general case, AlIn_2As_2 is a semiconductor at 0 GPa and 16 GPa and becomes metallic at 26 GPa. Again, from the results of Table II and Fig. 12, we know that the H_5 equation can represent the hardness of the system at 0 GPa and 16 GPa, while H_4 describes the hardness of the system at 26 GPa. In the absence of pressure, the monoclinic phase of AlIn_2As_2 has the maximum hardness (indicated by the grey curve). With a pressure of 16 GPa, the hardness is still expressed by H_5 , but the hardness decreases by almost half, especially for BaIn_2As_2 . At a pressure of 26 GPa, the hardness of the system increases again and is expressed by H_4 . We suggest that the change in hardness may have a necessary relationship to the structural phase transition. Overall, our predicted hardness of the AlIn_2As_2 material is not high, well below the experimental 96 GPa for diamond [66], but close to that of ZnO (7.2 GPa) [55], which is also a hexagonal phase.

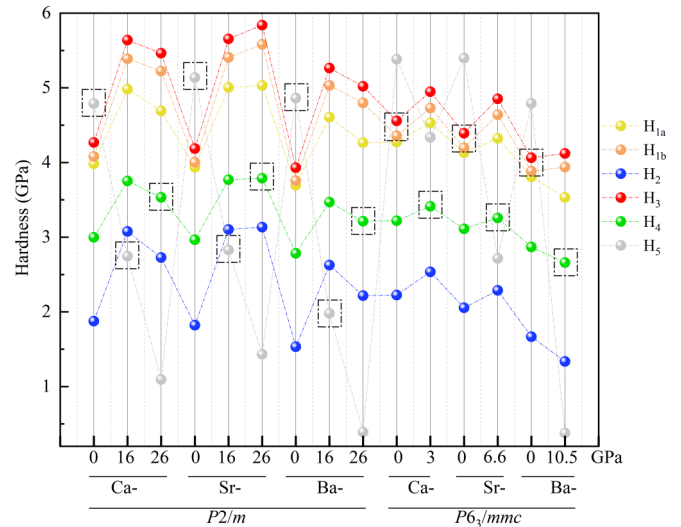


FIG. 12. Comparison of hardness parameters of AlIn_2As_2 hexagonal phase ($P6_3/mmc$) and monoclinic phase ($P2/m$) under different pressures.

In order to observe more comprehensively the effect of pressure on the overall hardness of the crystal, we calculated 3D hardness distributions for BaIn_2As_2 as an example (see Figs. 13). The left and right columns of Fig. 13 show the hardness distributions of monoclinic phase BaIn_2As_2 at 0 GPa and 26 GPa, respectively. The hardness distribution is symmetric about the x axis when no pressure is applied [see Fig. 13(a)], and the symmetry of the hardness distribution is broken when 26 GPa pressure is applied [see Fig. 13(d)]. Such an asymmetric transition can be observed more clearly in the side (yz plane) of Figs. 13(b) and 13(e). The range of coordinates and the intensity of the contours in Figs. 13(a) and 13(d) allow determining that the maximum hardness of the 0 GPa crystal is higher than 26 GPa, consistent with the hardness relationship predicted quantitatively earlier. In addition, it can be found that the pressure application induces a shift in the hardness distribution of BaIn_2As_2 from clustering in the center of the crystal to dispersion in the y direction. Figures 13(c) and 13(f) show the projection of hardness in the xy plane. A comparison of the localized peak in Fig. 13(c) with the “fishtail” hardness relationship in Fig. 13(f) shows that pressure does weaken the hardness localization.

e. Analysis of the degree of $\Delta F - T$ linear correlation

We are concerned that at high temperatures (≥ 2500 K), the free energy difference of the pressure-absent AlIn_2As_2 system exhibits almost a linear decrease with temperature and has different slopes (see the enlarged figure in the upper right of Fig. S15(b) within the SM [30]). The temperature dependence of the energy difference between the two structural phases changes from parabolic to linear, and this monotonically decreasing relationship indicates that the phase transition from hexagonal to monoclinic has fully realized at ultrahigh temperatures. The degree of tilt of the curve depends on the A atomic radius size. To better illustrate the linearity, we performed an error analysis of

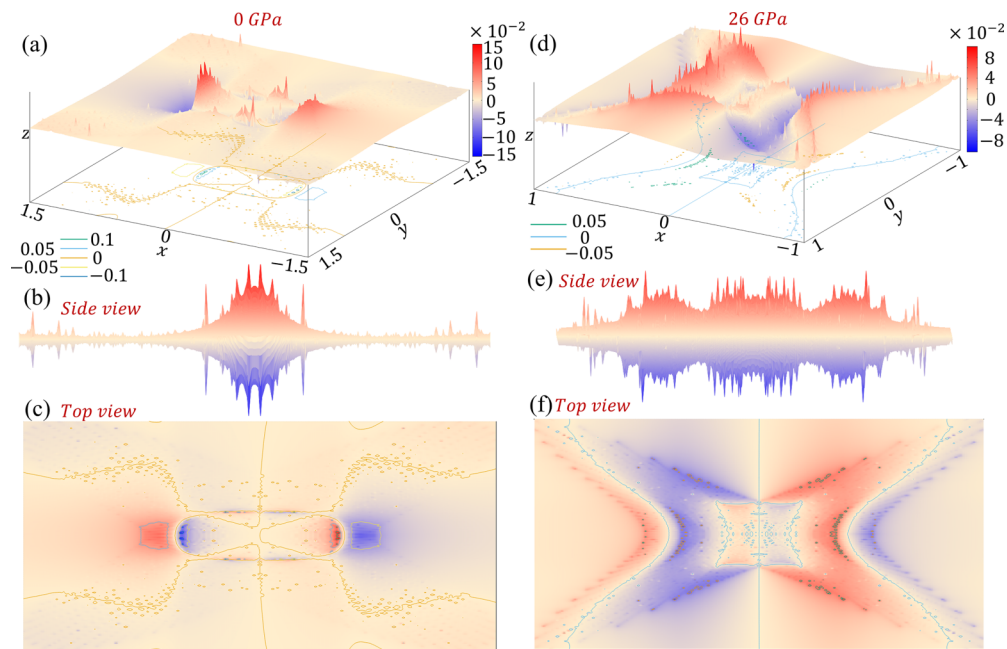


FIG. 13. Hardness distribution of the BaIn_2As_2 monoclinic phase structure under 0 and 26 GPa pressures.

the slopes over the full range (0–3000 K) with the high-temperature linear slopes of the three systems, and the results are shown in Fig. S16 within the SM [30]. From the marked slope errors of 5% of the temperature values (2400 K, 2450 K, and 2420 K for CaIn_2As_2 , SrIn_2As_2 and

BaIn_2As_2 , respectively), it can be seen that, within the error tolerance, the three systems show a linear slope after temperatures above 2500 K. The slope is linear for all three systems after the temperature above 2500 K within the error tolerance.

-
- [1] M. Arguilla, N. Cultrara, Z. Baum, S. Jiang, R. Ross, and J. Goldberger, EuSn_2As_2 : An exfoliatable magnetic layered Zintl–Klemm phase, *Inorg. Chem. Front.* **4**, 378 (2017).
- [2] H. Li, S.-Y. Gao, S.-F. Duan, Y.-F. Xu, K.-J. Zhu, S.-J. Tian, J.-C. Gao, W.-H. Fan, Z.-C. Rao, J.-R. Huang, J.-J. Li, D.-Y. Yan, Z.-T. Liu, W.-L. Liu, Y.-B. Huang, Y.-L. Li, Y. Liu, G.-B. Zhang, P. Zhang, T. Kondo *et al.*, Dirac Surface States in Intrinsic Magnetic Topological Insulators EuSn_2As_2 and $\text{MnBi}_{2n}\text{Te}_{3n+1}$, *Phys. Rev. X* **9**, 041039 (2019).
- [3] L. Zhao, C. Yi, C.-T. Wang, Z. Chi, Y. Yin, X. Ma, J. Dai, P. Yang, B. Yue, J. Cheng, F. Hong, J.-T. Wang, Y. Han, Y. Shi, and X. Yu, Monoclinic EuSn_2As_2 : A Novel High-Pressure Network Structure, *Phys. Rev. Lett.* **126**, 155701 (2021).
- [4] J.-T. Wang, C. Wang, and C. Chen, Pressure-densified new rhombohedral phase of EuSn_2As_2 , *Phys. Rev. B* **104**, L220101 (2021).
- [5] G. Hua, S. Nie, Z. Song, R. Yu, G. Xu, and K. Yao, Dirac semimetal in type-IV magnetic space groups, *Phys. Rev. B* **98**, 201116(R) (2018).
- [6] J. Krishna, T. Nautiyal, and T. Maitra, First-principles study of electronic structure, transport, and optical properties of EuCd_2As_2 , *Phys. Rev. B* **98**, 125110 (2018).
- [7] M. C. Rahn, J.-R. Soh, S. Francoual, L. S. I. Veiga, J. Stempffer, J. Mardegan, D. Y. Yan, Y. F. Guo, Y. G. Shi, and A. T. Boothroyd, Coupling of magnetic order and charge transport in the candidate Dirac semimetal EuCd_2As_2 , *Phys. Rev. B* **97**, 214422 (2018).
- [8] C. Niu, N. Mao, X. Hu, B. Huang, and Y. Dai, Quantum anomalous Hall effect and gate-controllable topological phase transition in layered EuCd_2As_2 , *Phys. Rev. B* **99**, 235119 (2019).
- [9] Y. Xu, Z. Song, Z. Wang, H. Weng, and X. Dai, Higher-Order Topology of the Axion Insulator EuIn_2As_2 , *Phys. Rev. Lett.* **122**, 256402 (2019).
- [10] O. Pozo, C. Repellin, and A. G. Grushin, Quantization in Chiral Higher Order Topological Insulators: Circular Dichroism and Local Chern Marker, *Phys. Rev. Lett.* **123**, 247401 (2019).
- [11] T. Sato, Z. Wang, D. Takane, S. Souma, C. Cui, Y. Li, K. Nakayama, T. Kawakami, Y. Kubota, C. Cacho, T. K. Kim, A. Arab, V. N. Strocov, Y. Yao, and T. Takahashi, Signature of band inversion in the antiferromagnetic phase of axion insulator candidate EuIn_2As_2 , *Phys. Rev. Res.* **2**, 033342 (2020).
- [12] S. Regmi, M. M. Hosen, B. Ghosh, B. Singh, G. Dhakal, C. Sims, B. Wang, F. Kabir, K. Dimitri, Y. Liu, A. Agarwal, H. Lin, D. Kaczorowski, A. Bansil, and M. Neupane, Temperature-dependent electronic structure in a higher-order topological insulator candidate EuIn_2As_2 , *Phys. Rev. B* **102**, 165153 (2020).
- [13] S. X. Riberolles, T. V. Trevisan, B. Kuthanazhi, T. Heitmann, F. Ye, D. C. Johnston, S. L. Bud’ko, D. H. Ryan, P. C. Canfield, A. Kreyssig *et al.*, Magnetic crystalline-symmetry-protected axion electrodynamics and field-tunable unpinned Dirac cones in EuIn_2As_2 , *Nat. Commun.* **12**, 999 (2021).

- [14] Y. Zhang, K. Deng, X. Zhang, M. Wang, Y. Wang, C. Liu, J.-W. Mei, S. Kumar, E. F. Schwier, K. Shimada, C. Chen, and B. Shen, In-plane antiferromagnetic moments and magnetic polaron in the axion topological insulator candidate EuIn_2As_2 , *Phys. Rev. B* **101**, 205126 (2020).
- [15] S. H. Shah, G. Murtaza, A. Baz, E. Algrafy, A. Laref, and N. A. Kattan, Study of anion replacement effect on SrCd_2X_2 ($X = \text{P, As, Sb, Bi}$) compounds by FPLAPW+lo, *Mater. Sci. Semiconduct. Process.* **119**, 105290 (2020).
- [16] J. M. DeStefano and L.-L. Wang, Pressure effect on band inversion in AECd_2As_2 ($A = \text{Ca, Sr, Ba}$), *Phys. Rev. B* **103**, 115207 (2021).
- [17] S. H. Shah, S. Khan, G. Murtaza, M. Amir Ali, A. Laref, E. Algrafy, and A. A. H. Ahmadini, Anion replacement effect on BaCd_2X_2 ($X = \text{P, As, Sb, Bi}$) compounds: A first principles study, *J. Solid State Chem.* **292**, 121589 (2020).
- [18] L.-Y. Rong, J.-Z. Ma, S.-M. Nie, Z.-P. Lin, Z.-L. Li, B.-B. Fu, L.-Y. Kong, X.-Z. Zhang, Y.-B. Huang, H.-M. Weng *et al.*, Electronic structure of SrSn_2As_2 near the topological critical point, *Sci. Rep.* **7**, 1 (2017).
- [19] K. Shinozaki, Y. Goto, K. Hoshi, R. Kiyama, N. Nakamura, A. Miura, C. Moriyoshi, Y. Kuroiwa, H. Usui, and Y. Mizuguchi, Thermoelectric properties of the As/P-Based Zintl compounds $\text{EuIn}_2\text{As}_{2-x}\text{P}_x$ ($x = 0-2$) and SrSn_2As_2 , *ACS Appl. Energy Mater.* **4**, 5155 (2021).
- [20] W.-T. Guo, Z. Huang, and J.-M. Zhang, The Zintl phase compounds AEIn_2As_2 ($\text{AE} = \text{Ca, Sr, Ba}$): Topological phase transition under pressure, *Phys. Chem. Chem. Phys.* **24**, 17337 (2022).
- [21] M. O. Ogunbunmi, S. Baranets, A. Childs, and S. Bobev, The Zintl phases AIn_2As_2 ($A = \text{Ca, Sr, Ba}$): New topological insulators and thermoelectric material candidates, *Dalton Trans.* **50**, 9173 (2021).
- [22] C.-Y. Pei, Y.-Y.-Y. Xia, J.-Z. Wu, Y. Zhao, L.-L. Gao, T.-P. Ying, B. Gao, N.-N. Li, W.-G. Yang, D.-Z. Zhang *et al.*, Pressure-induced topological and structural phase transitions in an antiferromagnetic topological insulator, *Chin. Phys. Lett.* **37**, 066401 (2020).
- [23] W.-T. Guo, L. Huang, Y. Yang, Z. Huang, and J.-M. Zhang, Pressure-induced topological quantum phase transition in the magnetic topological insulator MnBi_2Te_4 , *New J. Phys.* **23**, 083030 (2021).
- [24] A. Rancati, N. Pournaghavi, M. F. Islam, A. Debernardi, and C. M. Canali, Impurity-induced topological phase transitions in Cd_3As_2 and Na_3Bi Dirac semimetals, *Phys. Rev. B* **102**, 195110 (2020).
- [25] W.-Z. Zheng, T.-Y. Zhao, A.-Q. Wang, D.-Y. Xu, P.-Z. Xiang, X.-G. Ye, and Z.-M. Liao, Strain-gradient induced topological transition in bent nanoribbons of the Dirac semimetal Cd_3As_2 , *Phys. Rev. B* **104**, 155140 (2021).
- [26] Y. Ruan, Y. Yang, Y. Zhou, L. Huang, G. Xu, K. Zhong, Z. Huang, and J.-M. Zhang, Band-structure engineering of the magnetically Cr-doped topological insulator Sb_2Te_3 under mechanical strain, *J. Phys.: Condens. Matter* **31**, 385501 (2019).
- [27] K. Y. Chen, B. S. Wang, J.-Q. Yan, D. S. Parker, J.-S. Zhou, Y. Uwatoko, and J.-G. Cheng, Suppression of the antiferromagnetic metallic state in the pressurized MnBi_2Te_4 single crystal, *Phys. Rev. Mater.* **3**, 094201 (2019).
- [28] W.-T. Guo, L. Huang, G.-G. Xu, K.-H. Zhong, J.-M. Zhang, and Z.-G. Huang, Pressure strain control of electronic structure of intrinsic magnetic topological insulator MnBi_2Te_4 , *Acta Phys. Sin.* **70**, 047101 (2021).
- [29] X.-R. Cheng, X.-Y. Kuang, H. Cheng, H. Tian, S.-M. Yang, M. Yu, X.-L. Dou, and A.-J. Mao, Strain-induced structural phase transition, electric polarization and unusual electric properties in photovoltaic materials CsMI_3 ($M = \text{Pb, Sn}$), *RSC Adv.* **10**, 12432 (2020).
- [30] See Supplemental Material at <http://link.aps.org/supplemental/10.1103/PhysRevB.108.094111> for the figures that help expand and extend the main manuscript. Includes 3D elastic modulus and 2D elastic modulus, heat capacity curves, free energy, entropy, and phonon group velocities in the x, y, z directions for the $P6_3/mmc$ space group and $P2/m$ space group at pressure. Phonon dispersion spectra for the $R3m$ and $P2/m$ space groups and tables of phonon frequencies for monoclinic phases are also provided.
- [31] G. Kresse and J. Hafner, *Ab initio* molecular dynamics for open-shell transition metals, *Phys. Rev. B* **48**, 13115 (1993).
- [32] G. Kresse and J. Furthmüller, Efficient iterative schemes for *ab initio* total-energy calculations using a plane-wave basis set, *Phys. Rev. B* **54**, 11169 (1996).
- [33] P. E. Blöchl, Projector augmented-wave method, *Phys. Rev. B* **50**, 17953 (1994).
- [34] J. P. Perdew, K. Burke, and M. Ernzerhof, Generalized Gradient Approximation Made Simple, *Phys. Rev. Lett.* **77**, 3865 (1996).
- [35] T. Streck and H. Jopek, Effective mechanical properties of concentric cylindrical composites with auxetic phase, *Phys. Status Solidi B* **249**, 1359 (2012).
- [36] M. Grujicic, R. Galgalikar, J. Snipes, R. Yavari, and S. Ramaswami, Multi-physics modeling of the fabrication and dynamic performance of all-metal auxetic-hexagonal sandwich-structures, *Materials and Design* **51**, 113 (2013).
- [37] T. Streck, H. Jopek, B. T. Maruszewski, and M. Nienartowicz, Computational analysis of sandwich-structured composites with an auxetic phase, *Phys. Status Solidi B* **251**, 354 (2014).
- [38] R. H. Baughman, J. M. Shacklette, A. A. Zakhidov, and S. Stafström, Negative Poisson's ratios as a common feature of cubic metals, *Nature (London)* **392**, 362 (1998).
- [39] X. Ren, X. Zhang, and Y. Xie, Research progress in auxetic materials and structures, *Chin. J. Theor. Appl. Mech.* **51**, 656 (2019).
- [40] A. Togo and I. Tanaka, First principles phonon calculations in materials science, *Scr. Mater.* **108**, 1 (2015).
- [41] Y. Oba, T. Tadano, R. Akashi, and S. Tsuneyuki, First-principles study of phonon anharmonicity and negative thermal expansion in ScF_3 , *Phys. Rev. Mater.* **3**, 033601 (2019).
- [42] Y. Wang, Y. Zhang, and C. Wolverton, First-principles studies of phase stability and crystal structures in Li-Zn mixed-metal borohydrides, *Phys. Rev. B* **88**, 024119 (2013).
- [43] J. Ojih, U. Onyekpe, A. Rodriguez, J. Hu, C. Peng, and M. Hu, Machine learning accelerated discovery of promising thermal energy storage materials with high heat capacity, *ACS Appl. Mater. Interfaces* **14**, 43277 (2022).
- [44] J. P. Watt, Hashin-shtrikman bounds on the effective elastic moduli of polycrystals with monoclinic symmetry, *J. Appl. Phys.* **51**, 1520 (1980).
- [45] J. F. Nye, *Physical Properties of Crystals* (Oxford University Press, Oxford, 1985).

- [46] R. Hill, The elastic behaviour of a crystalline aggregate, *Proc. Phys. Soc. A* **65**, 349 (1952).
- [47] W. Voigt, *Lehrbuch der Kristallphysik* (Springer, Stuttgart, 1966).
- [48] A. Reuss, Berechnung der Fließgrenze von Mischkristallen auf Grund der Plastizitätsbedingung für Einkristalle, *Z. angew. Math. Mech.* **9**, 49 (1929).
- [49] C. Zener, *Elasticity and Anelasticity of Metals* (University of Chicago, Chicago, 1948).
- [50] D. H. Chung and W. R. Buessem, The elastic anisotropy of crystals, *J. Appl. Phys.* **38**, 2010 (1967).
- [51] S. I. Ranganathan and M. Ostoja-Starzewski, Universal Elastic Anisotropy Index, *Phys. Rev. Lett.* **101**, 055504 (2008).
- [52] C. M. Kube, Elastic anisotropy of crystals, *AIP Adv.* **6**, 095209 (2016).
- [53] L. Kleinman, Deformation potentials in silicon. I. Uniaxial strain, *Phys. Rev.* **128**, 2614 (1962).
- [54] L. Bao, D. Qu, Z. Kong, and Y. Duan, Anisotropies in elastic properties and thermal conductivities of trigonal TM_2C (TM = V, Nb, Ta) carbides, *Solid State Sci.* **98**, 106027 (2019).
- [55] X. Jiang, J. Zhao, and X. Jiang, Correlation between hardness and elastic moduli of the covalent crystals, *Comput. Mater. Sci.* **50**, 2287 (2011).
- [56] D. M. Teter, Computational alchemy: The search for new superhard materials, *MRS Bull.* **23**, 22 (1998).
- [57] X. Jiang, J. Zhao, A. Wu, Y. Bai, and X. Jiang, Mechanical and electronic properties of B_12 -based ternary crystals of orthorhombic phase, *J. Phys.: Condens. Matter* **22**, 315503 (2010).
- [58] N. Miao, B. Sa, J. Zhou, and Z. Sun, Theoretical investigation on the transition-metal borides with Ta_3B_4 -type structure: A class of hard and refractory materials, *Comput. Mater. Sci.* **50**, 1559 (2011).
- [59] X.-Q. Chen, H. Niu, D. Li, and Y. Li, Modeling hardness of polycrystalline materials and bulk metallic glasses, *Intermetallics* **19**, 1275 (2011).
- [60] A. Ivanovskii, Hardness of hexagonal AlB_2 -like diborides of s , p and d metals from semi-empirical estimations, *Int. J. Refract. Met. Hard Mater.* **36**, 179 (2013).
- [61] S. Singh, L. Lang, V. Dovale-Farelo, U. Herath, P. Tavadze, F.-X. Coudert, and A. H. Romero, Mechelastic: A python library for analysis of mechanical and elastic properties of bulk and 2D materials, *Comput. Phys. Commun.* **267**, 108068 (2021).
- [62] S. Yalameha, Z. Nourbakhsh, and D. Vashaee, Elatools: A tool for analyzing anisotropic elastic properties of the 2D and 3D materials, *Comput. Phys. Commun.* **271**, 108195 (2021).
- [63] S. Singh, I. Valencia-Jaime, O. Pavlic, and A. H. Romero, Elastic, mechanical, and thermodynamic properties of Bi-Sb binaries: Effect of spin-orbit coupling, *Phys. Rev. B* **97**, 054108 (2018).
- [64] R. Gaillac, P. Pullumbi, and F.-X. Coudert, Elate: An open-source online application for analysis and visualization of elastic tensors, *J. Phys.: Condens. Matter* **28**, 275201 (2016).
- [65] S. Ivantchev, E. Kroumova, G. Madariaga, J. M. Pérez-Mato, and M. I. Aroyo, *SUBGROUPGRAPH*: A computer program for analysis of group-subgroup relations between space groups, *J. Appl. Crystallogr.* **33**, 1190 (2000).
- [66] C. A. Klein and G. F. Cardinale, Young's modulus and Poisson's ratio of CVD diamond, *Diam. Relat. Mater.* **2**, 918 (1993).